

Decoding post-transcriptional regulatory networks by RNA-linked CRISPR screening in human cells

Received: 23 July 2024

Accepted: 11 April 2025

Published online: 29 May 2025

Patrick J. Nugent  ^{1,2}, Heungwon Park  ¹, Cynthia L. Wladyka ³, James N. Yelland  ¹, Sayantani Sinha  ⁴, Katharine Y. Chen  ^{1,2}, Christine Bynum ^{1,5}, Grace Quarterman ^{1,5}, Stanley C. Lee ⁴, Andrew C. Hsieh  ^{3,6} & Arvind Rasi Subramaniam  ^{1,7} 

 Check for updates

RNAs undergo a complex choreography of metabolic processes that are regulated by thousands of RNA-associated proteins. Here we introduce ReLiC, a scalable and high-throughput RNA-linked CRISPR approach to measure the responses of diverse RNA metabolic processes to knockout of 2,092 human genes encoding all known RNA-associated proteins. ReLiC relies on an iterative strategy to integrate genes encoding Cas9, single-guide RNAs (sgRNAs) and barcoded reporter libraries into a defined genomic locus. Combining ReLiC with polysome fractionation reveals key regulators of ribosome occupancy, uncovering links between translation and proteostasis. Isoform-specific ReLiC captures differential regulation of intron retention and exon skipping by SF3B complex subunits. Chemogenomic ReLiC screens decipher translational regulators upstream of messenger RNA (mRNA) decay and identify a role for the ribosome collision sensor GCN1 during treatment with the anti-leukemic drug homoharringtonine. Our work demonstrates ReLiC as a powerful framework for discovering and dissecting post-transcriptional regulatory networks in human cells.

After transcription, RNAs undergo several metabolic events such as splicing, editing, localization, translation and decay inside cells. These RNA processes are executed by ribonucleoprotein complexes composed of RNA-binding proteins (RBPs), adaptor proteins and regulatory factors. Over 2,000 human genes encode proteins that are part of ribonucleoprotein complexes^{1,2}. Mutations in RNA-associated proteins occur in many human diseases such as cancer, neurodegeneration and developmental disorders³.

Cross-linking-based biochemical approaches can identify RBP–RNA interactions² but not their functional effect on RNA metabolism.

RBPs can increase, decrease or leave unchanged metabolic events on their target RNA depending on their affinity, location and other associated factors^{4,5}. Many RBPs also associate with multiple protein complexes and participate in several distinct RNA metabolic events⁶. Conversely, protein factors that do not directly bind RNA can still affect RNA metabolism by regulating the interactions between RNAs and RBPs or by controlling the cellular level and activity of RBPs⁷.

Unbiased genetic screening can identify cellular factors regulating RNA metabolism but are limited in their current form. CRISPR screens using indirect phenotypes such as cell growth and fluorescent protein

¹Basic Sciences Division and Computational Biology Section of the Public Health Sciences Division, Fred Hutchinson Cancer Center, Seattle, WA, USA.

²Molecular and Cellular Biology Graduate Program, University of Washington, Seattle, WA, USA. ³Human Biology Division, Fred Hutchinson Cancer Center, Seattle, WA, USA. ⁴Translational Science and Therapeutics Division, Fred Hutchinson Cancer Center, Seattle, WA, USA. ⁵Department of Biology, Spelman College, Atlanta, GA, USA. ⁶Department of Medicine and Department of Genome Sciences, University of Washington, Seattle, WA, USA.

⁷Department of Biochemistry and Department of Genome Sciences, University of Washington, Seattle, WA, USA.  e-mail: rasi@fredhutch.org

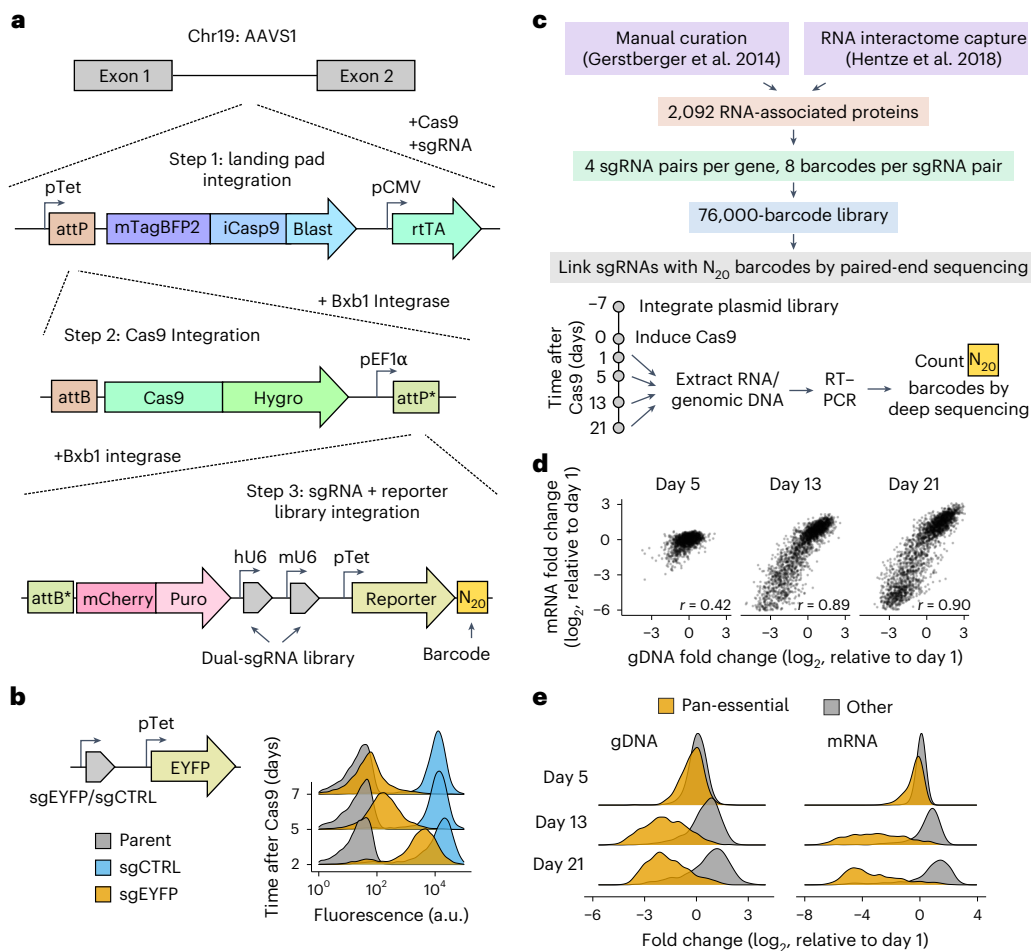


Fig. 1 | Development of ReLiC screening. **a**, Strategy for genomic integration of the Bxb1 landing pad, SpCas9 dual sgRNAs and barcoded RNA reporters. BFP, blue fluorescent protein; chr, chromosome; hygro, hygromycin; rtTA, doxycycline-inducible trans-activator; pCMV, cytomegalovirus early promoter. **b**, Validation of Cas9 activity. sgEYFP refers to an EYFP-targeting sgRNA, and sgCTRL is a nontargeting control. Histograms represent fluorescence of 10,000 cells as measured by flow cytometry. ‘Time after Cas9 (days)’ refers to time (days) after addition of doxycycline to induce Cas9 expression. a.u., arbitrary

units. **c**, Strategy for ReLiC sgRNA library design and validation. **d**, Correlated change in barcode frequency between genomic DNA (gDNA) and mRNA after Cas9 induction. Each point corresponds to a gene knockout. Fold changes are median centered across all sgRNA pairs in the library. Gene-level fold changes are median values across all detected sgRNAs for each gene. r refers to the Pearson correlation coefficient. **e**, Essential gene knockouts are depleted in genomic DNA and mRNA after Cas9 induction. Pan-essential genes from the DepMap database ($n = 745$) and remaining genes ($n = 1,401$) are shown as separate histograms.

levels are difficult to engineer and interpret for many RNA metabolic events^{8,9} due to potential false positives^{10,11} and genetic compensatory mechanisms¹². CRISPR perturbations followed by pooled single-cell RNA sequencing can capture RNA phenotypes such as steady-state levels, polyadenylation status and decay rates^{13–15}. But these transcriptome-wide approaches have limited flexibility to study different types of RNA processes, show bias toward highly expressed RNAs and remain costly and labor intensive to scale beyond a few dozen perturbations. Thus, genome-scale screening approaches to identify the RNA-centric functions of human proteins, which also have the flexibility to capture diverse RNA metabolic events, are highly desirable.

Results

Development of RNA-linked CRISPR screening in human cells

We reasoned that combining CRISPR-based perturbations with barcoded RNA readouts provides a general approach to study the genetic control of RNA processes in human cells. Indeed, RNA interference screens in human cells¹⁶ and CRISPR interference screens in *Saccharomyces cerevisiae*^{17,18} have linked perturbations to barcoded transcriptional readouts. Lentiviral delivery, commonly used for CRISPR screening in human cells, scrambles single-guide RNA (sgRNA)-barcode linkages due to template switching during reverse transcription

(RT)¹⁹ and results in variable expression of RNA barcodes due to random genomic integration²⁰. To avoid these limitations, we used an iterative, Bxb1-mediated site-specific integration strategy to stably express doxycycline-inducible SpCas9 (Cas9 hereafter), sgRNAs and barcoded RNA reporters from a defined genomic locus (Fig. 1a). Using an EYFP reporter, we confirmed its uniform expression and Cas9-mediated depletion in HEK293T (Fig. 1b) and U2OS (Extended Data Fig. 1a,b) cells.

To identify post-transcriptional regulators, we targeted 2,092 human genes encoding known RNA-associated proteins^{1,2} (Fig. 1c). We used a dual-sgRNA design with random N₂₀ barcodes in a modular vector allowing insertion of arbitrary RNA reporters (Extended Data Fig. 1c). Our final library targeted 2,190 genes with four sgRNA pairs per gene, including nontargeting and essential gene-targeting controls (Supplementary Table 1). We linked the N₂₀ barcodes to sgRNAs by paired-end deep sequencing of the cloned plasmid library. We then integrated this library into HEK293T cells and counted barcodes in the genomic DNA and transcribed RNA by deep sequencing (Fig. 1c and Extended Data Fig. 1d). We recovered a median of eight barcodes per sgRNA pair (henceforth referred to as sgRNAs) with at least one barcode for 99% of sgRNAs and 100% of all genes (Extended Data Fig. 1e), thus capturing the diversity of our input library.

To test whether sgRNA-linked barcodes capture fitness effects, we counted barcodes in genomic DNA and messenger RNA (mRNA) after Cas9 induction (Supplementary Table 6). Barcode counts showed little systematic change 5 days after Cas9 induction (Fig. 1d, left). However, on days 13 and 21 after Cas9 induction, barcode counts for a subset of sgRNAs were strongly depleted in both genomic DNA and mRNA in a highly correlated manner (Fig. 1d, middle and right). The magnitude of depletion was correlated across distinct barcode sets for each gene (Extended Data Fig. 1f), indicating the assay's technical reproducibility. Barcodes in both genomic DNA and mRNA corresponding to annotated essential genes ($n = 745$) were depleted at days 13 and 21 relative to other genes targeted by our library ($n = 1,401$; Fig. 1e). Thus, ReLiC captures both the identity and fitness effect of genetic perturbations solely from sequencing of barcodes in mRNA and genomic DNA.

ReLiC identifies regulators of mRNA translation

We first applied ReLiC to study translation, an RNA process that is not directly accessible in existing CRISPR screening methods. We combined ReLiC with polysome profiling^{21–23} to separate mRNAs based on their ribosome occupancy. We used a β-globin reporter²⁴ as a model of a well-translated mRNA (Fig. 2a), inserted random barcodes into its 3' untranslated region (UTR) and confirmed that over 75% of the β-globin mRNA was in polysome fractions (Fig. 2b). We then cloned the β-globin reporter into our ReLiC plasmid library, integrated the plasmids into HEK293T cells, induced Cas9 for 7 days and fractionated cell lysates (Fig. 2a). After counting sgRNA-linked barcodes in pooled fractions, we used MAGeCK²⁵ to identify sgRNAs that significantly altered the ratio of barcode counts between heavy (H) or light (L) polysomes and monosomes (M) (Supplementary Table 7). Polysome-to-monomosome ratios for individual sgRNAs were highly reproducible ($r = 0.92$ and 0.80 for H/M and L/M, respectively) between replicate experiments (Extended Data Fig. 2a). We used a false discovery rate (FDR) threshold of 0.05 and a minimum of three concordant sgRNAs for calling gene hits that altered polysome-to-monomosome ratios (Supplementary Table 8).

In total, 304 and 207 gene hits decreased heavy polysome-to-monomosome and light polysome-to-monomosome ratios, respectively (Fig. 2c). Thirty-seven gene hits increased the heavy polysome-to-monomosome ratio, while two increased the light polysome-to-monomosome ratio (Fig. 2c). A total of 176 gene hits overlapped between the heavy and light polysome ratios, indicating a largely concordant effect of gene knockouts on different polysome fractions. The skewed distribution of gene hits with more perturbations decreasing ribosome occupancy likely arises from the efficient translation of β-globin mRNA in unperturbed cells (Fig. 2b). Consistent with heavy polysome fractions containing better-translated mRNAs, heavy polysome-to-monomosome ratios were more sensitive to perturbations with more gene hits and larger effect sizes than light polysome-to-monomosome ratios (Fig. 2c). We therefore focused on heavy polysome-to-monomosome ratios for further analyses.

Gene hits that decreased polysome-to-monomosome ratios were highly enriched for cytoplasmic ribosomal proteins and ribosome biogenesis factors (Extended Data Fig. 2b). On average, knockout of large ribosomal proteins and biogenesis factors decreased polysome-to-monomosome ratios more than knockout of small ribosomal proteins and biogenesis factors (Fig. 2d). Sequencing of barcodes in supernatant fractions revealed that knockout of small ribosomal proteins and biogenesis factors led to increased barcode representation in the supernatant relative to monosomes, while knockout of large ribosomal proteins and biogenesis factors had the opposite effect (Fig. 2e). This observation is consistent with small ribosomal subunit depletion preventing association between mRNAs and ribosomes, while large ribosomal subunit depletion still allows scanning by one or more small ribosomal subunits. Indeed, barcode ratios between supernatant and polysome revealed comparable effects of small and large ribosomal perturbations (Extended Data Fig. 2c).

Depletion of most translation initiation factors also decreased heavy polysome-to-monomosome ratios, but their effects were generally smaller than the effect of ribosomal protein depletion (Fig. 2f). Some initiation factor subunits not classified as hits (open circles, Fig. 2f) still had multiple sgRNAs that decreased the heavy polysome-to-monomosome ratio but either fell just below our gene-level FDR threshold (EIF4G1) or did not meet our stringent criterion of three distinct sgRNAs with significant effects (EIF2S2, EIF4E). In the case of the 12-subunit EIF3 and associated EIF3J, the seven subunits A–E, G and I called as hits are the same ones that severely reduce polysome-to-monomosome ratio and fitness when depleted by small interfering RNA in HeLa cells²⁶. While most canonical initiation factors emerged as hits upon comparison of the polysome fraction to either the monosome or the supernatant fractions, a few genes such as *XRN1*, *DDX6* and *SNTB1* emerged as hits only in the polysome-to-supernatant comparison (Extended Data Fig. 2d). Aminoacyl transfer RNA (tRNA) synthetase knockouts had mild and variable effects on ribosomal occupancy (Fig. 2f), presumably reflecting a balance between their direct effect on elongation and indirect effect on initiation through GCN2 and EIF2α phosphorylation²⁷.

We identified several knockouts outside the core translation machinery with decreased polysome-to-monomosome ratio (Fig. 2f). Subunits of the CCR4–NOT complex (CNOT1, CNOT2, CNOT3 and CNOT7), which has been implicated in a wide range of RNA metabolic processes²⁸, emerged as hits in our screen. Knockout of proteasome and TRiC chaperonin subunits led to substantially reduced polysome-to-monomosome ratios, comparable in magnitude to knockout of core translation initiation factors (Fig. 2f). We validated these effects by creating individual knockout lines and observed reduced bulk polysome-to-monomosome ratios after 3 days of proteasomal or chaperonin depletion (Extended Data Fig. 2e). These complexes did not arise as hits only due to their essentiality, as knockout of other essential cellular complexes such as RNA polymerase II and SF3A and SF3B (SF3) did not reduce the polysome-to-monomosome ratio (Fig. 2f). While neither the proteasome nor the TRiC chaperonin complex has been directly associated with translational regulation, they play a critical role in maintaining cellular proteostasis by coordinating their activities with translation^{29,30}. Our results suggest a reciprocal regulation of translation in response to changes in proteasomal and chaperonin capacity.

Relation between ribosome occupancy and growth fitness

Ribosome occupancy on mRNAs is often correlated with cellular growth rate, with slower growth accompanied by lower polysome-to-monomosome ratio across different growth conditions and organisms^{26,31,32}. Our measurements of both depletion of barcodes and their polysome distribution across thousands of gene perturbations allowed testing the generality of the relationship between ribosome occupancy and growth. Across all perturbations, a decrease in the polysome-to-monomosome ratio was positively correlated with barcode depletion in both mRNA and genomic DNA but had a wide distribution (Extended Data Fig. 2f). However, gene groups corresponding to different molecular complexes had characteristically distinct relationships between ribosome occupancy and barcode depletion. Perturbing ribosomal proteins and biogenesis factors resulted in the largest decrease in the polysome-to-monomosome ratio relative to fitness, followed by EIF3 (Fig. 2g and Extended Data Fig. 2g). Perturbing proteasomal subunits produced a smaller but still significant decrease in ribosome occupancy, while perturbing RNA polymerase II subunits did not alter ribosome occupancy despite their significant effects on barcode depletion (Fig. 2g and Extended Data Fig. 2g). Hence, the coupling between growth rate and ribosome occupancy in human cells is not invariant across all perturbations but depends on the pathway or the molecular process that leads to growth limitation.

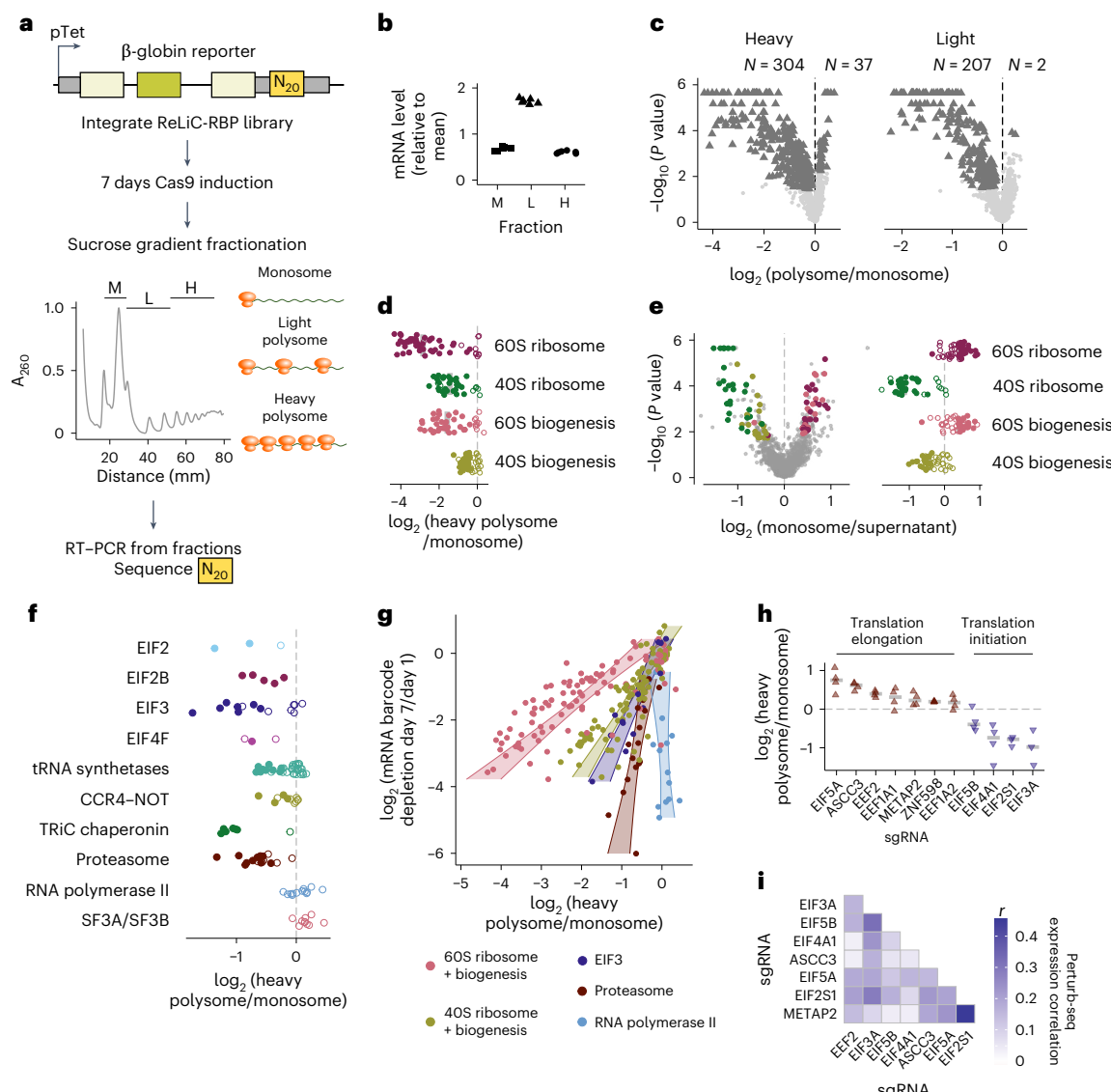


Fig. 2 | Polysome ReLiC identifies regulators of mRNA translation. **a**, Strategy for combining ReLiC and polysome fractionation. A_{260} , absorbance at 260 nm. **b**, Reporter distribution across polysome fractions in unperturbed cells. Points correspond to relative mRNA level in each fraction for distinct 3' UTR barcodes ($n = 6$) for the β -globin reporter. **c**, Change in polysome-to-monosome ratio after 7 days of Cas9 induction. Each point corresponds to a gene knockout. Horizontal axis indicates the median of polysome-to-monosome ratios of barcode counts across all detected sgRNAs for each gene. Number of genes with FDR < 0.05 and decreased or increased polysome-to-monosome ratio is indicated with N . Individual gene hits are highlighted in dark gray triangles. All other genes are shown as light gray circles. **d**, Change in polysome-to-monosome ratio for ribosomal protein and ribosome biogenesis genes. Closed circles correspond to gene hits (FDR < 0.05 with three or more concordant sgRNAs). **e**, Change in monosome-to-supernatant ratio for ribosomal protein and ribosome biogenesis

genes. Left: equivalent to **c** but for monosome/supernatant. Ribosomal protein and ribosome biogenesis hits are highlighted. Right: equivalent to **d** but for monosome/supernatant. Vertical axes in **c,e** indicate P values from a permutation test as calculated with MAGECK. **f**, Change in polysome-to-monosome ratio for protein groups and complexes. Closed and open circles denote gene hits and non-hits, similar to **d**. **g**, Comparison of ribosome occupancy and mRNA depletion. Points correspond to genes belonging to one of the highlighted groups. Shaded areas correspond to 95% confidence intervals for a linear fit. **h**, Barcode ratios between polysome fractions for individual translation factors. Each point corresponds to a distinct sgRNA, and gray bars denote the median value across detected sgRNAs for that gene. **i**, Correlation of expression profiles as measured by Perturb-seq¹³. r refers to the Pearson correlation coefficient. EEF1A1, EEF1A2 and ZNF598 depletions did not induce strong transcriptional responses; so they are excluded from the visualization.

Regulatory factors that increase ribosome occupancy

We next examined the small group of gene knockouts that increased the heavy polysome-to-monosome ratio (Fig. 2h, brown triangles). Knockout of *EEF2*, *EIF5A* and *EEF1A1* increased the polysome-to-monosome ratio, consistent with their role in promoting translation elongation. Intriguingly, the ribosome-associated quality control factor *ASCC3* was the top gene hit for increased heavy polysome-to-monosome ratio ($\log_2(H/M) = 0.62$, FDR = 1×10^{-4}). As *ASCC3* is involved in splitting stalled ribosomes on mRNAs³³, its presence here suggests that even well-translated mRNAs such as that for β -globin undergo some degree

of ribosome stalling and quality control. Furthermore, knockout of the ribosome collision sensor *ZNF598*, which acts upstream of *ASCC3* (ref. 33), also increased ribosome occupancy ($\log_2(H/M) = 0.19$, FDR = 0.06, $P = 0.007$). Knockout of *METAP2*, which removes methionine from the N terminus of nascent polypeptides, increased ribosome occupancy ($\log_2(H/M) = 0.22$, FDR = 0.001, $P = 3 \times 10^{-4}$), pointing to an effect of nascent peptide processing on the kinetics of mRNA translation.

Finally, we asked whether differential effects of gene perturbations on ribosome occupancy as measured by polysome-to-monosome ratios are reflected in their cellular transcriptional response. Using a

genome-scale Perturb-seq dataset¹³, we correlated and clustered the transcriptional profiles of translation factor perturbations that had concordant or discordant effects on ribosome occupancy (Fig. 2*i*). Perturbations with concordant effects on ribosome occupancy (Fig. 2*h*) did not show a higher correlation with each other than with perturbations with discordant effects on ribosome occupancy. For example, depletion of METAP2 and EIF2S1 (EIF2α), which are direct interactors³⁴, had a markedly higher correlation in the transcriptional responses even though these gene knockouts had discordant effects on ribosome occupancy (Fig. 2*h*). Thus, the effects of gene perturbations on ribosome occupancy measured by ReLiC are distinct from their downstream transcriptional responses.

Isoform-specific splicing screens using ReLiC

Existing screening approaches to study RNA splicing require careful design of fluorescent protein reporters¹⁰ and can result in high false positive and negative rates¹¹. We reasoned that ReLiC will allow us to directly measure the ratio of different splice isoforms carrying the same barcode, thereby capturing the effect of the linked sgRNA perturbation on splicing. To test this idea, we used the same β-globin reporter as in our translation screen (Fig. 3*a*) and confirmed the canonical isoform with three exons as the most abundant one (Fig. 3*b*). We then performed three isoform-specific screens for regulators that increase intron 1 retention, intron 2 retention or exon 2 skipping (Fig. 3*a*). After collecting RNA 1, 3, 5 and 7 days after Cas9 induction, we selectively amplified each isoform along with the barcode (Fig. 3*c*). We measured the ratio of barcode counts between each isoform and the total RNA pool and used an FDR threshold of 0.05 and a minimum of three concordant sgRNAs for calling gene hits (Supplementary Table 8). For all three isoforms, the number of gene hits progressively increased with longer duration of Cas9 induction (Extended Data Fig. 3*a*). Fewer gene knockouts increased the exon 2-skipped isoform in comparison to the two intron-retained isoforms at all time points (Extended Data Fig. 3*a*). Effect sizes of gene hits were reproducible across distinct barcode sets for each gene (Extended Data Fig. 3*b*) and specific to each isoform (Extended Data Fig. 3*c*).

The three isoform-specific screens identified both common and unique sets of gene hits that were evident by automated gene ontology analysis (Fig. 3*d*) and by manual inspection (Fig. 3*e*). Gene hits in the two intron retention screens were dominated by core spliceosome components and splicing-associated factors (yellow circles and triangles, Fig. 3*e*). Spliceosome hits were distributed throughout the splicing cycle starting from the tri-small nuclear (sn)ribonucleoprotein (snRNP) complex that is required to form the catalytically active spliceosome and included members from most known spliceosomal subcomplexes³⁵. Our screen also identified *trans* regulators of spliceosomal function such as CDK11B, a recently identified activator of the SF3B complex³⁶, and BRF2, an RNA polymerase III subunit required for transcription of U6 snRNA.

Retention of intron 1 was promoted by an additional group of gene knockouts that were enriched for mRNA translation and nuclear RNA exosome factors (red and brown triangles, Fig. 3*e*). Loss of ribosomal proteins and translation factors might inhibit nonsense-mediated decay (NMD) of the intron1-retained isoform, while the effect of nuclear RNA exosome components might be indirect through their role in ribosome biogenesis. While retention of either intron 1 or intron 2 will generate a premature termination codon (PTC), only the intron 1-retained isoform will have a splice junction and an associated exon–junction complex downstream of the PTC, which is a well-known trigger for NMD³⁷. Consistent with a role for NMD, exon–junction complex components (MAGOH, EIF4A3, RBM8A) and RNA export factors (NCBP1, NCBP2) emerged as hits only in the intron 1 retention screen (Fig. 3*e*), and several NMD factors such as UPF2 and SMG1 increased intron 1 retention even though they fell below our FDR threshold for calling hits (Supplementary Table 8).

Differential effects of SF3B complex subunits on splicing

In contrast to intron retention, perturbations increasing exon 2 skipping were enriched for a narrow set of splicing factors. Components of the U2 snRNP, most notably several members of the SF3 complex, were among the top hits (purple squares, Fig. 3*e*), suggesting that their depletion allows some degree of splicing but impairs the correct selection of splice sites. This is consistent with the subtle alterations in exon skipping caused by disease-causing mutations in the SF3B complex³⁸. Exon 2 skipping was also promoted by perturbing components involved in nuclear protein import (green squares, Fig. 3*e*), presumably through their effect on nuclear import of U2 snRNP proteins after their synthesis in the cytoplasm. Perturbing individual components of the seven-subunit SF3B complex³⁹ had distinct effects on exon skipping and intron retention (Fig. 3*f*), even though all seven subunits are essential for cell growth (Extended Data Fig. 3*d*). Exon 2 skipping was greatly increased upon loss of the subunits SF3B1, SF3B2, SF3B3 and SF3B5, slightly increased by loss of SF3B7 (PHF5A) and unaffected by loss of SF3B4 and SF3B6 (Fig. 3*f*). Intron 2 retention was increased by loss of SF3B6 and SF3B7, while intron 1 retention was increased by loss of SF3B1, SF3B2 and SF3B5 (Fig. 3*f*). By contrast, loss of the activating helicase AQR increased the retention of both introns 1 and 2 (brown markers, Fig. 3*f*).

We next examined how the differential effects of SF3B subunit depletion on β-globin reporter splicing extend to endogenous mRNAs. To this end, we generated HEK293T cell lines with the subunits SF3B5 and SF3B6, which affected distinct splicing events in our screen, individually depleted. We also targeted AQR, a top hit in both our intron retention screens, as a positive control and included a nontargeting control sgRNA (FLUC). We performed RNA-seq 4 days after Cas9 induction to identify endogenous splicing events that are particularly sensitive to the respective genetic perturbations. Loss of SF3B5 increased skipping of 45 annotated cassette exons by 10% or higher (Fig. 3*g*). Loss of SF3B6 or AQR affected the skipping of less than ten cassette exons at the same effect size, while all three splicing factors increased aberrant retention of a similar number of distinct introns (Fig. 3*g*). Interestingly, for genes such as *RPL24* and *RPL41*, increased intron retention and exon skipping upon SF3B5 loss occurred at distinct splice sites within the same transcriptional unit (Fig. 3*h,j*). In summary, the differential effects of SF3B subunits on splicing of the β-globin reporter extend to endogenous mRNAs, with a subset of SF3B subunits playing a more prominent role in regulating exon skipping.

ReLiC screen for regulators of mRNA quality control

We reasoned that sequencing mRNA barcodes using ReLiC provides a general approach to identify regulators of mRNA quality control pathways independent of their effect on protein expression. To test this idea, we modified our β-globin reporter to add a PTC at position 39 in the second exon (Fig. 4*a*), which is known to trigger NMD²⁴. At steady state, mRNA levels of the PTC-containing reporter were strongly reduced relative to a reporter with a normal termination codon (NTC; Extended Data Fig. 4*a*). To measure mRNA effects specific to the PTC and NTC reporters, we combined our ReLiC-RBP library with a dual-barcoding strategy¹⁷ to normalize barcode counts for the reporter of interest relative to those of the mCherry puromycin (puro) selection marker within each cell (Fig. 4*a*). We collected RNA 7 days after Cas9 induction and counted mRNA barcodes for the PTC and NTC β-globin reporters and the mCherry-puro marker.

We identified 90 gene hits (FDR < 0.05, three sgRNAs with concordant effects) for which knockout increased levels of the PTC reporter relative to the mCherry-puro marker (Fig. 4*b* and Extended Data Fig. 4*c*). We did not obtain any hits that increased mRNA levels of the NTC reporter, as expected from its higher mRNA stability (Fig. 4*b* and Extended Data Fig. 4*c*). Several core components of the NMD pathway (UPF1, UPF2, SMG1, SMG5, SMG7, ETF1) were among the gene hits for the PTC reporter, indicating our ability to identify NMD-specific factors

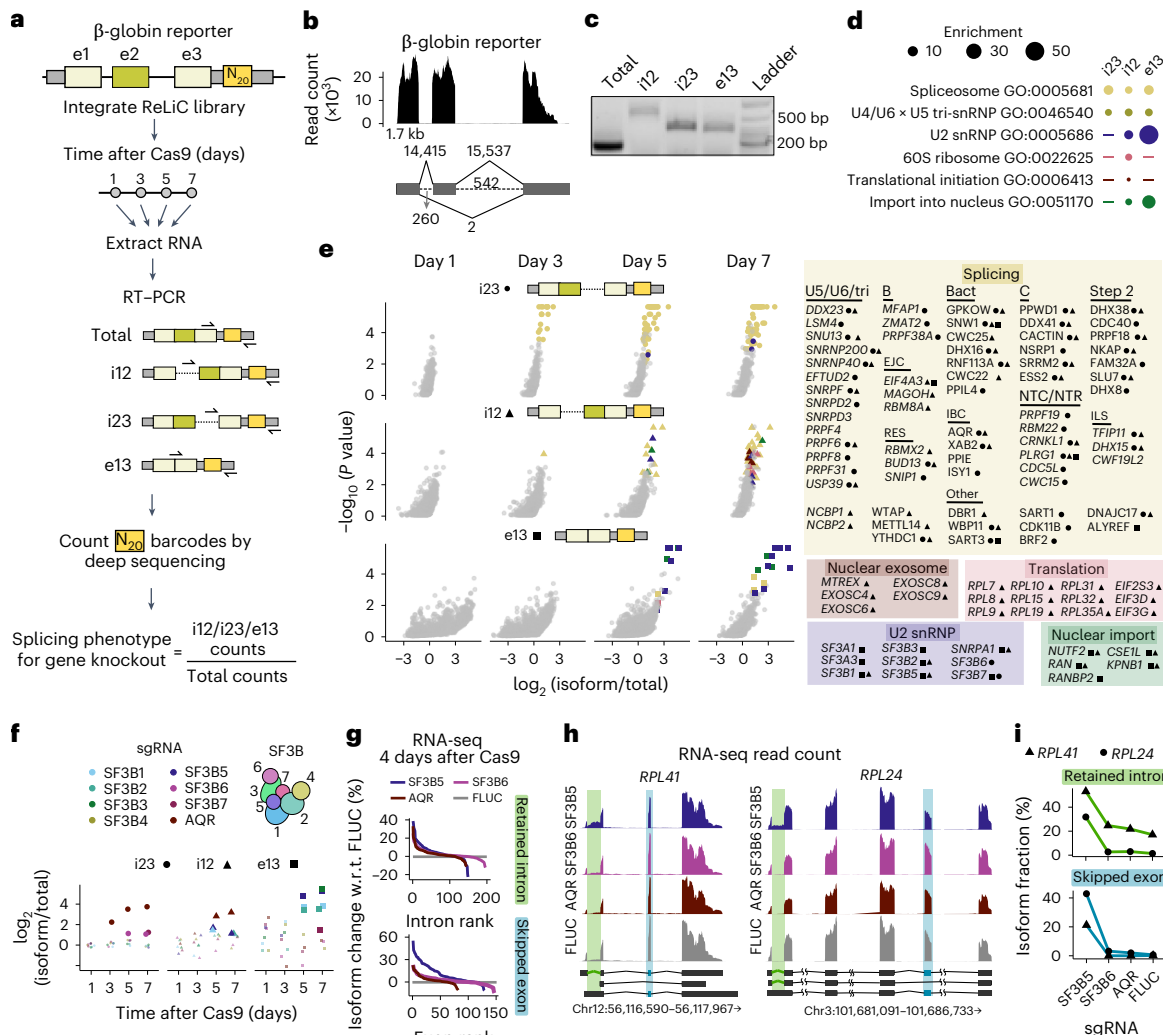


Fig. 3 | Isoform-specific splicing screens using ReLiC. **a**, Schematic of ReLiC splicing screens. Location of RT primer and PCR primers used for PCR amplification of barcodes in each isoform are shown as black arrows. i12, intron 1 retention; i23, intron 2 retention; e, exon; e13, exon 2 skipping. **b**, Relative abundance of β -globin reporter splice isoforms as measured by RNA-seq. Top: RNA-seq coverage. Bottom: read counts mapping to each splice junction and intron. **c**, Selective amplification of barcodes linked to splice isoforms. Agarose gel lanes show RT-PCR products of expected size for the different isoforms. **d**, Gene ontology (GO) analysis. Fold enrichment of selected cellular processes and components 7 days after Cas9 induction. En dashes indicate gene ontology terms with FDR > 0.05. **e**, Identity of splicing regulators. Each point corresponds to a gene knockout. Isoform ratios are median values across all detected sgRNAs for each gene after median centering across all sgRNAs in the library. Individual panels correspond to days after Cas9 induction (horizontal) and isoform screens (vertical). Marker shape denotes isoform identity, and marker color denotes one of five highlighted gene groups. Genes with FDR < 0.05 and belonging to one

(Fig. 4b, pink circles). Other NMD-associated factors such as SMG6 and EIF4A3 fell just below the FDR threshold but still significantly (MAGECK P value < 0.05) increased mRNA levels of the PTC reporter. Remarkably, a large proportion of gene hits for the PTC reporter encoded core factors involved in various steps of mRNA translation (Fig. 4b, squares, triangles and diamonds and Extended Data Fig. 4b). These included both small and large ribosomal proteins, ribosome biogenesis factors, translation initiation factors and aminoacyl-tRNA synthetases. EIF2, EIF2B and EIF3 subunits but not EIF4F subunits emerged as hits (Extended Data Fig. 4d), despite having similar effects on growth fitness (Extended Data Fig. 4e). Furthermore, acute chemical inhibition

of the highlighted groups are listed in the legend. EJC, exon junction complex; RES, retention and splicing complex; Bact, activated B complex; NTC, nineteen complex; NTR, NTC-related complex; IBC, intron-binding complex; ILS, intron lariat spliceosome. **f**, Relative reporter isoform levels upon SF3B complex perturbations. AQR is shown as a positive control hit for intron retention. FDR < 0.05 is indicated by large markers, and FDR ≥ 0.05 is indicated by small markers. **g**, Change in endogenous splicing isoforms upon SF3B complex perturbations. RNA-seq was performed 4 days after inducing Cas9. Changes in intron retention or cassette exon skipping were calculated across all Ensembl-annotated transcripts and ranked by decreasing magnitude of change with respect to (w.r.t.) the FLUC control sample. **h**, Examples of endogenous isoform changes. Changes in retained introns and skipped exons are highlighted in green and blue rectangles, respectively. Schematics at the bottom correspond to Ensembl isoforms with the highlighted retained intron and skipped exon events. **i**, Quantification of isoform fraction for the endogenous intron retention and exon-skipping events in **h**.

Chemical and genetic modifier screens using ReLiC

Our NMD screen also identified gene hits involved in endoplasmic reticulum (ER) and mitochondrial homeostasis (Fig. 4b, \times markers). This is consistent with phosphorylation of EIF2 α upon perturbing ER and mitochondrial homeostasis leading to NMD inhibition⁴⁰. To identify regulators of NMD acting through EIF2 α phosphorylation,

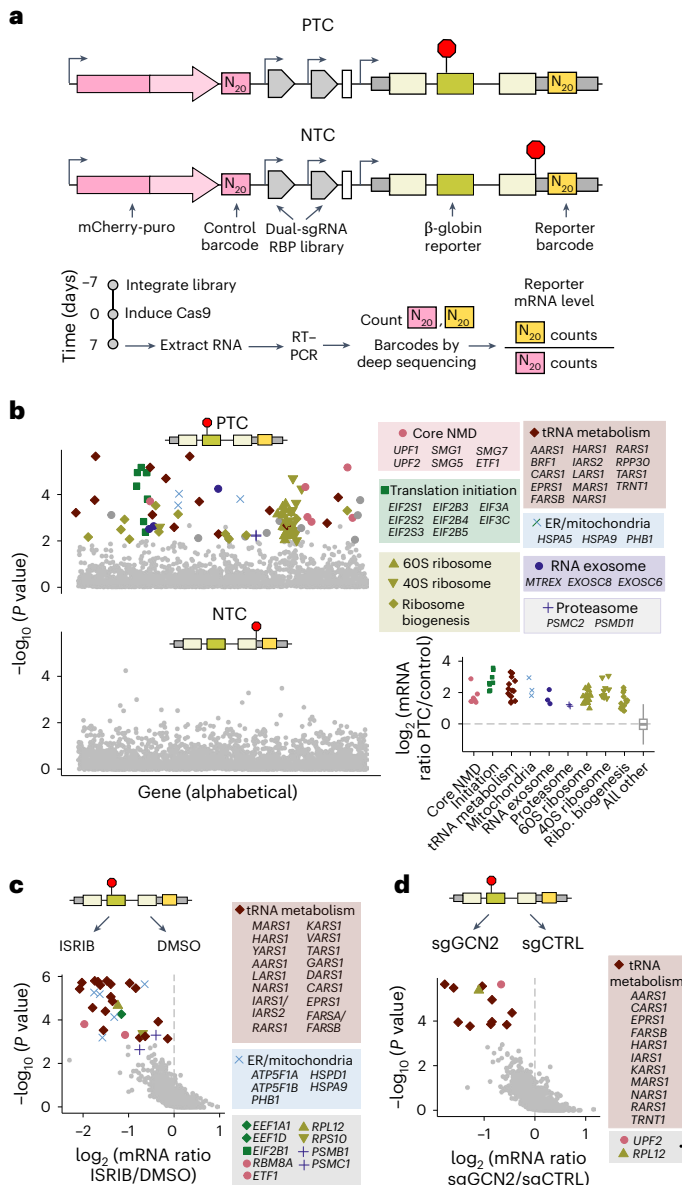


Fig. 4 | Dissecting cotranslational quality control using chemogenomic ReLiC screening. **a**, Dual-barcode strategy for measuring reporter mRNA levels. Red octagons denote stop codons. **b**, Gene hits from dual-barcode NMD screen. Gene hits ($FDR < 0.05$) within one of the six highlighted gene groups are listed in the legend. Genes are arranged alphabetically along the horizontal axis. Bottom right: reporter mRNA level of the highlighted hits for the PTC reporter relative to the control mCherry-puro reporter. Box plot indicates median (center), interquartile range (box) and $3 \times$ interquartile range (whiskers) of the relative reporter mRNA level across all detected genes in the experiment. ER, endoplasmic reticulum; Ribo., ribosome. **c**, Chemical modifier screen with ISRB. **d**, Genetic modifier screen with GCN2 depletion. mRNA fold changes and hits in **c**, **d** were calculated using MaGeCK as in **b** but with an FDR threshold of 0.01. Vertical axes in **b**–**d** indicate P values from a permutation test as calculated by MAGECK. Marker colors and shapes in **c**, **d** denote the highlighted gene groups from **b**.

we adapted ReLiC to perform a chemical modifier screen using the small molecule ISRB, which renders translation insensitive to EIF2 α phosphorylation⁴¹. After inducing Cas9 for 6 days, we treated a ReLiC cell pool expressing the PTC reporter with ISRB or dimethylsulfoxide (DMSO) for 48 h, collected RNA and counted barcodes. We identified 30 gene knockouts ($FDR < 0.01$) that decreased mRNA levels of the PTC reporter upon ISRB treatment relative to the DMSO control (Fig. 4c). These gene hits included several ER- and mitochondrion-localized

proteins (Fig. 4c, \times markers), consistent with their knockout inhibiting NMD through EIF2 α phosphorylation.

Knockout of several aminoacyl-tRNA synthetases also decreased PTC reporter levels upon ISRB treatment (Fig. 4c, diamonds), suggesting that their depletion inhibits NMD through phosphorylation of EIF2 α rather than by decreasing translation elongation. To test this hypothesis, we performed a genetic modifier screen using ReLiC to deplete the EIF2 α kinase GCN2, which is activated by uncharged tRNAs accumulating upon inhibition of aminoacyl-tRNA synthetases^{42,43}. We transduced the ReLiC cell pool with lentiviruses expressing either GCN2-targeting or nontargeting sgRNAs, induced Cas9 for 7 days, collected RNA and counted barcodes. Of the 12 gene hits ($FDR < 0.01$) with lower PTC reporter levels upon GCN2 depletion (Fig. 4d), ten were aminoacyl-tRNA synthetases (Fig. 4d, diamonds), thus confirming their action through GCN2-mediated EIF2 α phosphorylation. Together, the above chemical and genetic modifier screens demonstrate the usefulness of ReLiC for dissecting the molecular pathways through which specific gene products regulate RNA processes.

GCN1 regulates cellular responses to an anti-leukemic drug

Homoharringtonine (HHT) is a Food and Drug Administration-approved chemotherapeutic that targets the ribosomal subunit to arrest initiating ribosomes at start codons and inhibit protein synthesis⁴⁴, but how cells respond to this translational arrest is not well understood. Given ReLiC's ability to identify regulators downstream of both mRNA translation and chemical perturbations, we sought to use this approach to probe the cellular response to HHT treatment. To this end, we performed ReLiC screens using an enhanced yellow fluorescent protein (EYFP) reporter (Fig. 5a). After inducing Cas9 for 7 days, we treated the cell pool with 1 μ M HHT or DMSO for 6 h before collecting RNA and counting barcodes.

Unlike our previous ReLiC screens in which we uncovered multiple gene hits and RNA metabolic pathways, a single gene, *GCN1*, emerged as a clear hit ($FDR < 0.05$), knockout of which increased EYFP mRNA levels during HHT treatment (Fig. 5b). GCN1 activates the kinase GCN2 to trigger EIF2 α phosphorylation in response to amino acid limitation⁴⁷. While GCN2 did not come up as a hit in our initial HHT screen, pharmacologic inhibition of GCN2 ablated the difference in EYFP mRNA levels between *GCN1*-KO and control cells (Extended Data Fig. 5a). GCN1 also binds collided ribosomes on mRNAs⁴⁸, which can trigger both degradation of the nascent peptide and the mRNA^{49,50}. As ribosome collisions also trigger the ribotoxic stress response through the kinase ZAK α that was not included in our original screen⁵¹, we measured p38 phosphorylation in wild-type and GCN1-depleted cells. HHT treatment increased p38 phosphorylation in GCN1-depleted cells (Fig. 5d) in a ZAK α -dependent manner (Extended Data Fig. 5b), while wild-type cells did not show a corresponding increase. By contrast, treatment with the elongation inhibitor anisomycin triggered p38 phosphorylation in both wild-type and GCN1-depleted cells (Fig. 5d).

Ribosome collisions induced by elongation inhibitors trigger upregulation of immediate early gene (IEG) mRNAs⁵². To test whether GCN1 regulates IEGs during HHT treatment, we performed RNA-seq on wild-type and GCN1-depleted cells after HHT treatment (Fig. 5e). HHT treatment for 6 h caused widespread changes in mRNA levels in both wild-type and GCN1-depleted cells with ~225 upregulated genes and ~450 downregulated genes (>2-fold change, $P < 0.05$). However, a small group of 60 genes, which included several IEGs such as *FOS*, *JUN* and *MYC*, were differentially upregulated in GCN1-depleted cells relative to wild-type cells (Fig. 5e). GCN1-depleted cells from the myeloid lineage AML cell line U937 also showed pronounced upregulation of IEGs upon HHT treatment (Extended Data Fig. 5c). Furthermore, pharmacologic inhibition of ZAK or GCN2 prevented IEG upregulation in GCN1-depleted cells during HHT treatment (Extended Data Fig. 5d). The ZAK-dependent increased p38 signaling and IEG upregulation in

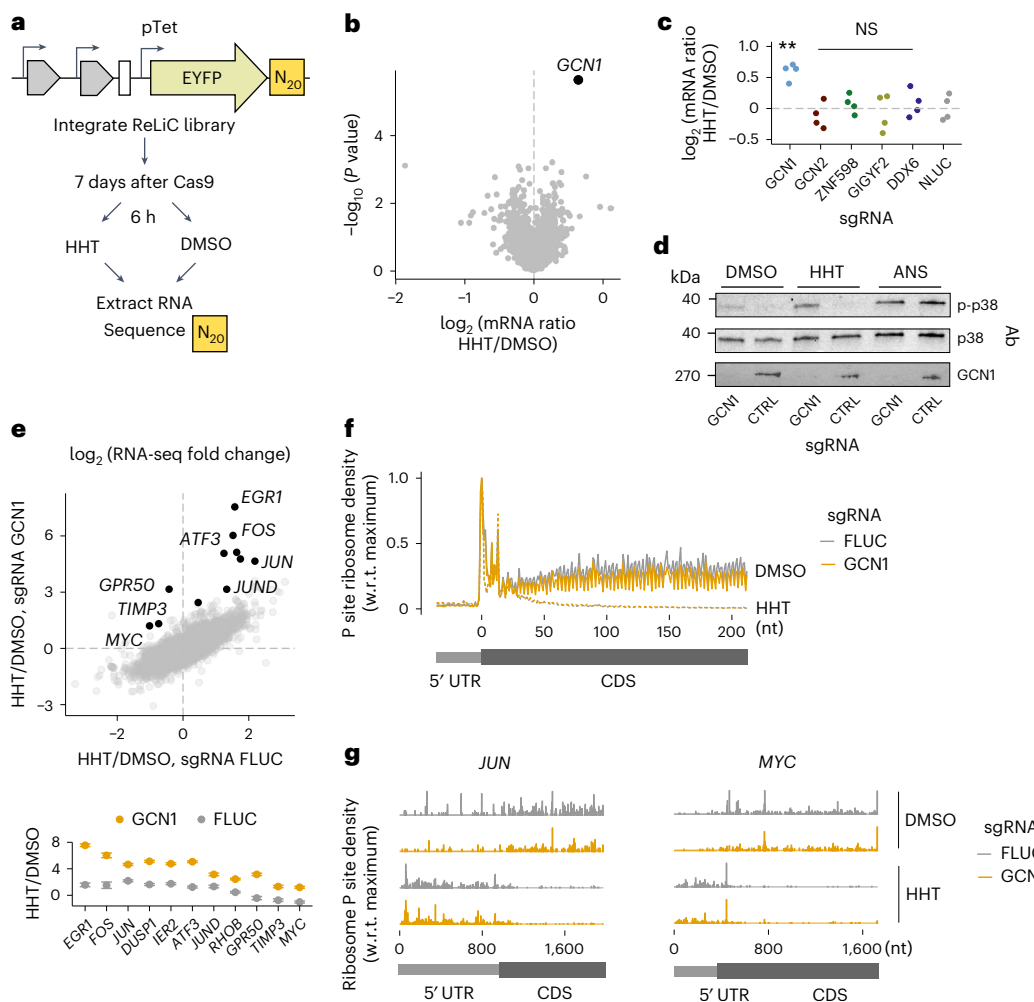


Fig. 5 | GCN1 regulates cellular responses to an anti-leukemic drug. **a**, Chemogenomic ReLiC screen using HHT. **b**, GCN1 regulates mRNA levels upon HHT treatment. Each point represents a gene knockout. Vertical axis indicates P values from a permutation test as calculated with MAGeCK. **c**, mRNA level changes upon HHT treatment for factors known to resolve ribosome collisions. Each point represents a distinct sgRNA pair from the ReLiC screen shown in **b**. **d**, P values comparing the indicated perturbations to cells expressing the nontargeting NLuc control sgRNA are from a two-sided t -test: **($0.001 < P < 0.01$), not significant (NS) ($P > 0.05$). **e**, Immunoblots for phosphorylation of p38

in HEK293T cells ±GCN1. Ab, antibody; ANS, anisomycin. **e**, GCN1-dependent changes in endogenous mRNA expression upon HHT treatment as measured by RNA-seq. Each point corresponds to a gene and represents the ratio of its mRNA levels between HHT and DMSO treatment. Black-highlighted points correspond to IEGs, which are also shown separately at the bottom. **f**, Metagene alignment of ribosome P site density in 5' UTR and coding sequence (CDS) across all detected transcripts as measured by ribosome profiling. nt, nucleotides. **g**, Ribosome P site density in 5' UTR and coding sequence of *JUN* and *MYC* transcripts. Horizontal axis indicates position along the transcript in nucleotides.

GCN1-depleted cells suggest a role for GCN1 in mitigating ribosome collisions during HHT treatment.

To test whether ribosome collisions occur on endogenous mRNAs during HHT treatment, we first performed polysome fractionation from both wild-type and GCN1-depleted cells (Extended Data Fig. 5e). Polysomes collapsed into monosomes after 1 h of HHT treatment, and nuclease-resistant peaks, indicative of collided ribosomes, were of comparable intensity in both wild-type and GCN1-depleted cells. Additionally, ribosome profiling under the same conditions did not show an obvious difference in average ribosome occupancy on mRNAs between wild-type and GCN1-depleted cells (Fig. 5f). Thus, ribosome collisions do not occur during HHT treatment at a level that is detectable by bulk biochemical fractionation and do not alter global ribosome occupancy on mRNAs. Nevertheless, highly expressed IEGs such as *JUN* and *MYC* exhibited extensive ribosome density throughout their 5' UTR during HHT treatment (Fig. 5g and Extended Data Fig. 5f). Furthermore, even in the absence of HHT, ribosomes initiate at multiple in-frame start codons on mRNAs of several IEGs such as *JUN*, *MYC* and *JUND*^{53–55}. Together, these observations suggest that GCN1 senses collisions on

these mRNAs between upstream scanning or elongating ribosomes and HHT-arrested initiating 80S ribosomes at downstream start codons.

Discussion

Our study demonstrates ReLiC, an RNA-linked CRISPR approach for genetic dissection of diverse post-transcriptional processes in human cells. ReLiC enables measuring the effect of thousands of gene perturbations on mRNA translation, splicing and decay, RNA processes that are not readily accessible to existing CRISPR screening methodologies. Our work reveals networks of molecular pathways, protein complexes and individual proteins regulating these processes. These measurements are consistent with known molecular mechanisms and illuminate the complex interplay between different post-transcriptional regulatory events.

ReLiC reveals the role of essential pathways and genes in RNA metabolism even when their knockout is deleterious to cell growth. Chemical perturbations that abrogate protein expression can still be probed for their genetic dependencies, as seen from our identification of GCN1's role during HHT treatment. ReLiC captures differential

effects of perturbations within the same protein complex such as between members of the SF3B complex and between large and small ribosomal proteins. Unlike biochemical strategies, ReLiC identifies both direct effectors and indirect regulators, as exemplified by the identification of translation-related pathways across our screens for ribosomal occupancy, splicing and mRNA decay.

ReLiC has complementary strengths and limitations for studying RNA metabolism compared to single-cell approaches. ReLiC can be readily combined with bulk RNA sequencing-based readouts, thus rendering diverse RNA phenotypes such as localization, condensation and editing amenable to genetic screening. Furthermore, ReLiC can be used to probe rare events such as aberrant splicing that are difficult to capture using existing single-cell approaches. Because ReLiC relies on targeted barcode sequencing, it can be executed at a genome scale in a cost-effective manner. Nevertheless, ReLiC depends on heterologously expressed reporters and thus requires follow-up studies on endogenous RNAs to establish transcriptome-wide significance. ReLiC also depends on non-lentiviral genomic integration to preserve linkage between sgRNA and reporter barcodes, which can limit its use to amenable cell types.

We anticipate that ReLiC can be extended to a broad range of biological settings, genetic perturbations and RNA classes. Applying ReLiC to diverse cell types, cell states and disease models will reveal differences in RNA metabolism that underlie cellular heterogeneity and disease progression. While we have used SpCas9 to induce gene knockouts, other effectors like base editors and prime editors can be readily incorporated into our modular workflow to identify the role of specific protein domains or regulatory elements on RNA metabolism with nucleotide resolution. Using noncoding, viral and synthetic RNAs instead of mRNA reporters in ReLiC has the potential to unlock novel RNA regulatory mechanisms and therapeutic strategies. Finally, expanding ReLiC from our RNA interactome-focused library to all protein-coding genes in the human genome will illuminate new interactions between RNA metabolism and other cellular processes.

Online content

Any methods, additional references, Nature Portfolio reporting summaries, source data, extended data, supplementary information, acknowledgements, peer review information; details of author contributions and competing interests; and statements of data and code availability are available at <https://doi.org/10.1038/s41592-025-02702-6>.

References

1. Gerstberger, S., Hafner, M. & Tuschl, T. A census of human RNA-binding proteins. *Nat. Rev. Genet.* **15**, 829–845 (2014).
2. Hentze, M. W., Castello, A., Schwarzl, T. & Preiss, T. A brave new world of RNA-binding proteins. *Nat. Rev. Mol. Cell Biol.* **19**, 327–341 (2018).
3. Gebauer, F., Schwarzl, T., Valcárcel, J. & Hentze, M. W. RNA-binding proteins in human genetic disease. *Nat. Rev. Genet.* **22**, 185–198 (2021).
4. Van Nostrand, E. L. et al. A large-scale binding and functional map of human RNA-binding proteins. *Nature* **583**, 711–719 (2020).
5. Ray, D. et al. A compendium of RNA-binding motifs for decoding gene regulation. *Nature* **499**, 172–177 (2013).
6. Schneider-Lunitz, V., Ruiz-Orera, J., Hubner, N. & van Heesch, S. Multifunctional RNA-binding proteins influence mRNA abundance and translational efficiency of distinct sets of target genes. *PLoS Comput. Biol.* **17**, e1009658 (2021).
7. England, W. E. et al. An atlas of posttranslational modifications on RNA binding proteins. *Nucleic Acids Res.* **50**, 4329–4339 (2022).
8. Przybyla, L. & Gilbert, L. A. A new era in functional genomics screens. *Nat. Rev. Genet.* **23**, 89–103 (2022).
9. Genolet, O., Ravid Lustig, L. & Schulz, E. G. Dissecting molecular phenotypes through FACS-based pooled CRISPR screens. *Methods Mol. Biol.* **2520**, 1–24 (2022).
10. Gonatopoulos-Pournatzis, T. et al. Genome-wide CRISPR–Cas9 interrogation of splicing networks reveals a mechanism for recognition of autism-misregulated neuronal microexons. *Mol. Cell* **72**, 510–524 (2018).
11. Scarborough, A. M. et al. SAM homeostasis is regulated by CFI_m-mediated splicing of MAT2A. *eLife* **10**, e64930 (2021).
12. El-Brolosy, M. A. et al. Genetic compensation triggered by mutant mRNA degradation. *Nature* **568**, 193–197 (2019).
13. Replogle, J. M. et al. Mapping information-rich genotype–phenotype landscapes with genome-scale Perturb-seq. *Cell* **185**, 2559–2575 (2022).
14. Kowalski, M. H. et al. Multiplexed single-cell characterization of alternative polyadenylation regulators. *Cell* **187**, 4408–4425 (2024).
15. Xu, Z., Sziraki, A., Lee, J., Zhou, W. & Cao, J. Dissecting key regulators of transcriptome kinetics through scalable single-cell RNA profiling of pooled CRISPR screens. *Nat. Biotechnol.* **42**, 1218–1223 (2024).
16. Herholt, A. et al. Pathway sensor-based functional genomics screening identifies modulators of neuronal activity. *Sci. Rep.* **8**, 17597 (2018).
17. Muller, R., Meacham, Z. A., Ferguson, L. & Ingolia, N. T. CiBER-seq dissects genetic networks by quantitative CRISPRi profiling of expression phenotypes. *Science* **370**, eabb9662 (2020).
18. Alford, B. D. et al. ReporterSeq reveals genome-wide dynamic modulators of the heat shock response across diverse stressors. *eLife* **10**, e57376 (2021).
19. Sack, L. M., Davoli, T., Xu, Q., Li, M. Z. & Elledge, S. J. Sources of error in mammalian genetic screens. *G3* **6**, 2781–2790 (2016).
20. Ellis, J. Silencing and variegation of gammaretrovirus and lentivirus vectors. *Hum. Gene Ther.* **16**, 1241–1246 (2005).
21. Warner, J. R., Knopf, P. M. & Rich, A. A multiple ribosomal structure in protein synthesis. *Proc. Natl Acad. Sci. USA* **49**, 122–129 (1963).
22. Noll, H., Staehelin, T. & Wettstein, F. O. Ribosomal aggregates engaged in protein synthesis: ergosome breakdown and messenger ribonucleic acid transport. *Nature* **198**, 632–638 (1963).
23. Gierer, A. Function of aggregated reticulocyte ribosomes in protein synthesis. *J. Mol. Biol.* **6**, 148–157 (1963).
24. Zhang, J., Sun, X., Qian, Y. & Maquat, L. E. Intron function in the nonsense-mediated decay of β-globin mRNA: indications that pre-mRNA splicing in the nucleus can influence mRNA translation in the cytoplasm. *RNA* **4**, 801–815 (1998).
25. Li, W. et al. MAGeCK enables robust identification of essential genes from genome-scale CRISPR/Cas9 knockout screens. *Genome Biol.* **15**, 554 (2014).
26. Wagner, S., Herrmannová, A., Šikrová, D. & Valášek, L. S. Human eIF3b and eIF3a serve as the nucleation core for the assembly of eIF3 into two interconnected modules: the yeast-like core and the octamer. *Nucleic Acids Res.* **44**, 10772–10788 (2016).
27. Darnell, A. M., Subramaniam, A. R. & O’Shea, E. K. Translational control through differential ribosome pausing during amino acid limitation in mammalian cells. *Mol. Cell* **71**, 229–243 (2018).
28. Collart, M. A. The Ccr4-Not complex is a key regulator of eukaryotic gene expression. *Wiley Interdiscip. Rev. RNA* **7**, 438–454 (2016).
29. Harper, J. W. & Bennett, E. J. Proteome complexity and the forces that drive proteome imbalance. *Nature* **537**, 328–338 (2016).
30. Frydman, J. Mechanism and function of the eukaryotic ring-shaped chaperonin TRiC/CCT. *Biophys. J.* **102**, 428a (2012).
31. Balakrishnan, R. et al. Principles of gene regulation quantitatively connect DNA to RNA and proteins in bacteria. *Science* **378**, eabk2066 (2022).

32. Metzl-Raz, E. et al. Principles of cellular resource allocation revealed by condition-dependent proteome profiling. *eLife* **6**, e28034 (2017).
33. Juszkiewicz, S., Speldewinde, S. H., Wan, L., Svejstrup, J. Q. & Hegde, R. S. The ASC-1 complex disassembles collided ribosomes. *Mol. Cell* **79**, 603–614 (2020).
34. Datta, B., Chakrabarti, D., Roy, A. L. & Gupta, N. K. Roles of a 67-kDa polypeptide in reversal of protein synthesis inhibition in heme-deficient reticulocyte lysate. *Proc. Natl Acad. Sci. USA* **85**, 3324–3328 (1988).
35. Wahl, M. C. & Lührmann, R. SnapShot: spliceosome dynamics I. *Cell* **161**, 1474–e1 (2015).
36. Hluchý, M. et al. CDK11 regulates pre-mRNA splicing by phosphorylation of SF3B1. *Nature* **609**, 829–834 (2022).
37. Cheng, J., Belgrader, P., Zhou, X. & Maquat, L. E. Introns are *cis* effectors of the nonsense-codon-mediated reduction in nuclear mRNA abundance. *Mol. Cell. Biol.* **14**, 6317–6325 (1994).
38. Darman, R. B. et al. Cancer-associated SF3B1 hotspot mutations induce cryptic 3' splice site selection through use of a different branch point. *Cell Rep.* **13**, 1033–1045 (2015).
39. Cretu, C. et al. Molecular architecture of SF3b and structural consequences of its cancer-related mutations. *Mol. Cell* **64**, 307–319 (2016).
40. Wang, D. et al. Inhibition of nonsense-mediated RNA decay by the tumor microenvironment promotes tumorigenesis. *Mol. Cell. Biol.* **31**, 3670–3680 (2011).
41. Sidrauski, C. et al. Pharmacological brake-release of mRNA translation enhances cognitive memory. *eLife* **2**, e00498 (2013).
42. Wek, S. A., Zhu, S. & Wek, R. C. The histidyl-tRNA synthetase-related sequence in the eIF-2 α protein kinase GCN2 interacts with tRNA and is required for activation in response to starvation for different amino acids. *Mol. Cell. Biol.* **15**, 4497–4506 (1995).
43. Dong, J., Qiu, H., Garcia-Barrio, M., Anderson, J. & Hinnebusch, A. G. Uncharged tRNA activates GCN2 by displacing the protein kinase moiety from a bipartite tRNA-binding domain. *Mol. Cell* **6**, 269–279 (2000).
44. Gandhi, V., Plunkett, W. & Cortes, J. E. Omacetaxine: a protein translation inhibitor for treatment of chronic myelogenous leukemia. *Clin. Cancer Res.* **20**, 1735–1740 (2014).
45. Fresno, M., Jiménez, A. & Vázquez, D. Inhibition of translation in eukaryotic systems by harringtonine. *Eur. J. Biochem.* **72**, 323–330 (1977).
46. Ingolia, N. T., Lareau, L. F. & Weissman, J. S. Ribosome profiling of mouse embryonic stem cells reveals the complexity and dynamics of mammalian proteomes. *Cell* **147**, 789–802 (2011).
47. Marton, M. J., Crouch, D. & Hinnebusch, A. G. GCN1, a translational activator of GCN4 in *Saccharomyces cerevisiae*, is required for phosphorylation of eukaryotic translation initiation factor 2 by protein kinase GCN2. *Mol. Cell. Biol.* **13**, 3541–3556 (1993).
48. Pochopien, A. A. et al. Structure of Gcn1 bound to stalled and colliding 80S ribosomes. *Proc. Natl Acad. Sci. USA* **118**, e2022756118 (2021).
49. Oltion, K. et al. An E3 ligase network engages GCN1 to promote degradation of translation factors on stalled ribosomes. *Cell* **186**, 346–362 (2023).
50. Müller, M. B., Kasturi, P., Jayaraj, G. G. & Hartl, F. U. Mechanisms of readthrough mitigation reveal principles of GCN1-mediated translational quality control. *Cell* **186**, 3227–3244 (2023).
51. Wu, C. C.-C., Peterson, A., Zinshteyn, B., Regot, S. & Green, R. Ribosome collisions trigger general stress responses to regulate cell fate. *Cell* **182**, 404–416 (2020).
52. Sinha, N. K. et al. EDF1 coordinates cellular responses to ribosome collisions. *eLife* **9**, e58828 (2020).
53. Hann, S. R., King, M. W., Bentley, D. L., Anderson, C. W. & Eisenman, R. N. A non-AUG translational initiation in c-myc exon 1 generates an N-terminally distinct protein whose synthesis is disrupted in Burkitt's lymphomas. *Cell* **52**, 185–195 (1988).
54. Short, J. D. & Pfarr, C. M. Translational regulation of the JunD messenger RNA. *J. Biol. Chem.* **277**, 32697–32705 (2002).
55. González-Sánchez, A. M., Castellanos-Silva, E. A., Díaz-Figueroa, G. & Cate, J. H. D. JUN mRNA translation regulation is mediated by multiple 5' UTR and start codon features. *PLoS ONE* **19**, e0299779 (2024).

Publisher's note Springer Nature remains neutral with regard to jurisdictional claims in published maps and institutional affiliations.

Springer Nature or its licensor (e.g. a society or other partner) holds exclusive rights to this article under a publishing agreement with the author(s) or other rightsholder(s); author self-archiving of the accepted manuscript version of this article is solely governed by the terms of such publishing agreement and applicable law.

© The Author(s), under exclusive licence to Springer Nature America, Inc. 2025

Methods

Plasmid construction

Plasmids used in this study are listed in Supplementary Table 2, which also includes accession numbers for plasmids deposited to Addgene. Oligonucleotides used in this study are listed in Supplementary Table 3. Detailed cloning steps for all plasmid vectors constructed for this study are described in Supplementary Methods. DNA fragments used for cloning were either excised out by restriction digestion or amplified by PCR from suitable templates. Fragments were assembled together using isothermal assembly and transformed into NEB 10-beta cells. All constructs were verified by restriction digestion and Sanger or long-read sequencing.

Cell culture

Cell lines used in this study are listed in Supplementary Table 4. HEK293T (RRID CVCL_0063, ATCC, CRL-3216) and U2OS (RRID CVCL_0042, ATCC, HTB-96) cells were cultured in DMEM medium (1×, with 4.5 g l⁻¹ D-glucose, L-glutamine, no sodium pyruvate, Gibco, 11965-092) supplemented with 10% FBS (Thermo, 26140079) and 1× penicillin–streptomycin (Gibco, 15140-122) and were passaged using 0.25% trypsin in EDTA (Gibco, 25200-056). HEK293T cell lines were authenticated by short tandem repeat analysis. U2OS cells were not authenticated. U937 cells (RRID CVCL_0007) were cultured in RPMI supplemented with 10% heat-inactivated FBS, penicillin–streptomycin and 1× GlutaMAX (Gibco, 35050-061). Cells were grown at 37 °C with 5% CO₂. Cell lines were periodically confirmed to be free of *Mycoplasma* contamination. For the ISRBIB chemical modifier screen, cells were treated with 200 nM ISRBIB or DMSO for 48 h after 5 days of Cas9 induction. For the genetic modifier screen with GCN2 depletion, cells were transduced with lentiviruses expressing either a GCN2-targeting sgRNA or a control sgRNA, followed by Cas9 induction for 7 days. For the HHT chemical modifier screen, ReLiC-RBP cell pools with the EYFP reporter were treated with 1 μM HHT or DMSO for 6 h after 7 days of Cas9 induction. For immunoblotting experiments, cells were treated with HHT (1 μM), anisomycin (ANS, 10 μM) or DMSO for 1 h. RNA-seq was performed after treatment with HHT (1 μM) or DMSO for 6 h. Ribosome profiling was performed on ±GCN1 cells after HHT (1 μM) or DMSO treatment for 1 h.

Generation of landing pad cell lines

To generate an initial attP landing pad line, HEK293T cells were transfected with landing pad plasmid (pPHHS232) and pASHS29 (AAVS1 T2 CRISPR in pX330 (ref. 56), Addgene, 72833) using polyethylenimine. U2OS cells were nucleofected with the same plasmids using the Nucleofector V kit (Lonza) in a Nucleofector 2b system. HEK293T cells were selected with 10 μg ml⁻¹ blasticidin S, added 96 h after transfection and maintained for 4 days. Blasticidin selection was omitted for U2OS cells. At this point, BFP expression was induced in all lines by adding 2 μg ml⁻¹ doxycycline. After doxycycline induction (24 h), the cultures were enriched for BFP⁺ cells using a FACSAria II flow cytometer (BD). The sorted BFP⁺ U2OS cells were kept as a polyclonal cell line (hsPN279). HEK293T landing pad clones were isolated by limiting dilution into 96-well plates. After isolating clones, two were pooled into a single cell line (hsPB126).

To integrate a cas9 expression cassette with an orthogonal attP* site into the initial attP landing pad clonal lines, hsPB126 was transfected with Cas9 landing pad plasmid (pPHHS800) and a Bxb1 expression plasmid (pPHHS115) using TransIT-LT1 reagent (Mirus) while hsPN279 was nucleofected with the same plasmids using the Nucleofector V kit. After transfection (72 h), hygromycin phosphotransferase was induced by adding 2 μg ml⁻¹ doxycycline, and then cells were selected with 150 μg ml⁻¹ hygromycin B, added 96 h after transfection. After 7 days, doxycycline and hygromycin B were removed from cells. At this point, the HEK293T cells were further selected using 10 μg ml⁻¹ blasticidin for 7 days, and this polyclonal cell line (hsPN266) was used for subsequent experiments. Instead of selecting with blasticidin, the

U2OS cells were further enriched for BFP⁺ cells using a FACSAria II flow cytometer (BD). The sorted BFP⁺ U2OS cells were kept as a polyclonal cell line (hsPN280).

Validation of reporter integration and Cas9 activity in landing pad cell lines

hsPN266 (HEK293T attP* cas9) cells were seeded at 70% confluence in a six-well or 12-well culture dish and transfected with 1 μg (six-well) or 200 ng (12-well) of Bxb1 expression vector (pPHHS115) and 2 μg (six-well) or 800 ng (12-well) of attB*-containing sgFLUC-EYFP or sgYFP-EYFP reporter plasmid (pPHHS885 and pPHHS886, respectively) using FuGENE HD (six-well) or Lipofectamine 2000 (12-well) reagent. A total of 1 × 10⁶ hsPN280 (U2OS attP* cas9) cells were nucleofected with 1 μg pPHHS115 and 2 μg pPHHS885 or pPHHS886 using the Nucleofector V kit. Each culture was selected with 2 μg ml⁻¹ puromycin, added 72 h after transfection. Flow cytometry was performed on a small split of cells from each culture not selected with puromycin to measure integration efficiency 7 days after transfection (Extended Data Fig. 1b). Puromycin selection was ended after 4 days on these cell lines (referred to as hsPN349, hsPN351, hsPN353, hsPN354). Twenty-four hours after ending puromycin selection, 2 μg ml⁻¹ doxycycline was added to induce Cas9 expression. After inducing Cas9, reporter expression was monitored over time by flow cytometry on the indicated days (Fig. 1b and Extended Data Fig. 1a).

sgRNA insert–barcode linkage sequencing

sgRNA insert–barcode linkages were determined at the step right after barcodes were added to the cloned sgRNA plasmid pool, before adding AmpR between the sgRNAs. A 422-bp amplicon containing both sgRNAs and 20 × N barcodes was generated from 1.5 ng of pPHHS932 plasmid by ten cycles of PCR using oKC196 and oPN726 primers and Phusion polymerase (Thermo). This product was cut out from a 1.5% agarose gel and cleaned using the Zymoclean Gel DNA Recovery Kit (Zymo). This sample was sequenced on an Illumina NextSeq 2000 using custom sequencing primers: oAS1701 for read 1 (26 cycles), oKC186 for index 1 (six cycles), oAS1702 for index 2 (20 cycles) and oKC185 for read 2 (75 cycles).

Integration of plasmid libraries into the landing pad

hsPN266 (HEK293T attP* cas9) cells were seeded at 60% confluence in one 15-cm dish per library. attB*-containing reporter library plasmid (20 μg) (pAS243, pAS244, pPHHS951) and 5 μg Bxb1 expression vector (pPHHS115) were transfected per 15-cm dish using the TransIT-LT1 reagent (Mirus). Each library was transfected into a single 15-cm dish and then expanded into four 15-cm dishes 48 h after transfection. Cells were selected with 2 μg ml⁻¹ puromycin, added 72 h after transfection. Puromycin selection was ended after 4 days, and library cell lines (referred to as hsPN305, hsPN306 and hsPN285) were contracted back into a single 15-cm dish. Twenty-four hours after ending puromycin selection, 2 μg ml⁻¹ doxycycline was added to induce Cas9 expression, and libraries were expanded into three 15-cm dishes, one each for RNA and genomic DNA collection the next day plus a third for continued propagation. This splitting procedure was repeated every other day from the propagation dish so that collections could be made throughout the duration of the screen. At no point were cultures bottlenecked to fewer than 5 × 10⁶ cells.

Library genomic DNA extraction

For each collection, reporter library genomic DNA was collected from one 50% confluent 15-cm dish of cells stably expressing the ReLiC library. Genomic DNA was collected using the Quick-DNA Miniprep kit (Zymo), following the manufacturer's instructions, with 2.5 ml of genomic DNA lysis buffer per 15-cm plate. Purified genomic DNA (30 μg) from each library sample was sheared into ~350-nucleotide-long fragments by sonication for 10 min on ice using a Diagenode Bioruptor.

Sheared genomic DNA was then transcribed in vitro into RNA (denoted gRNA below and in analysis code) starting from the T7 promoter region in the insert cassette using the HiScribe T7 High Yield RNA Synthesis Kit (NEB). Transcribed gRNA was cleaned using the RNA Clean and Concentrator kit (Zymo).

Library mRNA extraction

For each collection, reporter library mRNA was collected from one 50–75% confluent 15-cm dish of cells stably expressing the ReLiC library. Total RNA was collected by using 3.5 ml TRIzol reagent (Thermo) to lyse cells directly on the plate, and then RNA was extracted from these lysates using the Direct-zol RNA Miniprep kit (Zymo) following the manufacturer's protocol. PolyA⁺ mRNA was extracted from total RNA using Oligo d(T)25 Magnetic Beads (NEB). Total RNA (30–50 µg) was used as polyA selection input for total barcode-counting libraries from each sample, while 10–12 µg was used as input for splicing or polysome fraction barcode-counting libraries. Four microliters of Oligo d(T)25 beads were used per 1 µg of total RNA input.

mRNA and genomic DNA barcode sequencing

PolyA-selected mRNA or in vitro transcribed gRNA (100–500 ng) from each library was reverse transcribed into cDNA using SuperScript IV reverse transcriptase (Thermo) following the manufacturer's protocol. For RT, we used a primer that binds downstream of the 20 × N reporter barcode: either oPN777 for mRNA barcode 1, oPN731 for gRNA barcode 1 or oPN779 for mRNA barcode 2. oPN777 and oPN779 contain a seven-nucleotide unique molecular identifier (UMI). Libraries for sequencing total levels of barcode 1 or barcode 2 in each sample were made in a single PCR step. For both barcodes, a 100–200-µl PCR was performed using Phusion polymerase (Thermo) for 20–25 cycles with cDNA template comprising one-fifth of the final volume, and oPN776 was used as a constant reverse primer that binds the Illumina P5 sequence present on oPN777 and oPN779. Indexed forward primers that bind a constant region upstream of each barcode were used to enable pooled sequencing of different samples (one of oPN730, oPN738, oPN809, oPN815–822 or oY1-14 for barcode 1 or one of oPN734, oPN739 or oPN823–825 for barcode 2). All these reactions generated a 181-bp amplicon that was cut out from a 2% agarose gel and cleaned using the Zymoclean Gel DNA Recovery Kit (Zymo).

For splicing screens, two rounds of PCR were performed. Round 1 was performed as a 50-µl PCR for 30 cycles, again with cDNA template comprising one-fifth of the final volume and oPN776 as a constant reverse primer. The forward primer for round 1 was chosen based on the measured splicing event: oPN841 for intron 1 retention, oPN789 for intron 2 retention or oAS2029 for exon 2 skipping. These generate 532-, 302- and 286-bp amplicons, respectively, which were cut out from a 2% agarose gel and cleaned using the Zymoclean Gel DNA Recovery Kit (Zymo), eluting in 15 µl. Round 2 PCR was then essentially the same as the single-step PCR for total barcode 1 sequencing, except reactions were 20 µl, used 4 µl of cleaned round 1 product as template and proceeded for five cycles.

Libraries were sequenced on an Illumina NextSeq 2000 using custom sequencing primers. Custom primers for barcode 1 were oAS1701 for read 1, oPN732 for index 1, oPN775 for index 2 and oPN731 for read 2. Custom primers for barcode 2 were oPN735 for read 1, oPN737 for index 1, oPN778 for index 2 and oPN736 for read 2. Read lengths varied between sequencing runs with 10% PhiX spiked in.

Polysome fractionation for ReLiC

After Cas9 induction, 293T cells expressing ReLiC libraries were passaged for 6 days. On day 6, lysates were prepared from each library at 30% confluence in a 15-cm dish. Cultures were treated with 100 µg ml⁻¹ cycloheximide for 5 min before collection, and then cells were trypsinized (including 100 µg ml⁻¹ cycloheximide) and pelleted at 300g for 5 min. Cell pellets were lysed on ice in 300 µl polysome lysis buffer

(10 mM Tris-HCl, pH 7.4 (Ambion), 132 mM NaCl (Ambion), 1.4 mM MgCl₂ (Ambion), 19 mM DTT (Sigma), 142 µg ml⁻¹ cycloheximide (Sigma), 0.1% Triton X-100 (Fisher), 0.2% NP-40 (Pierce), 607 U ml⁻¹ SUPERase-In RNase Inhibitor (Invitrogen) with periodic vortex mixing. Lysates were clarified by centrifugation at 9,300g for 5 min, and supernatants were transferred to fresh tubes. This total lysate was split into two parts: 50 µl for total mRNA isolation and 250 µl for polysome profiling. For each sample, the 250-µl lysate fraction was layered onto a 10–50% (wt/vol) linear sucrose gradient (Fisher) containing 2 mM DTT (Sigma) and 100 µg ml⁻¹ heparin (Sigma). The gradients were centrifuged at 235,000g (37,000 rpm) for 2.5 h at 4 °C in a Beckman SW 41 Ti rotor in Seton 7030 ultracentrifuge tubes. After centrifugation, samples were fractionated using a Biocomp Gradient Station by upward displacement into collection tubes through a Bio-Rad EM-1UV monitor (Bio-Rad) for continuous measurement of the absorbance at 260 nm. TRIzol reagent (820 µl, Invitrogen) was added to each RNA fraction. Total (input), supernatant (fractions 1 and 2), monosome-associated (fractions 4 and 5), low polysome-associated (fractions 6–9) and high polysome-associated (fractions 10–13) samples were pooled as necessary, and RNA was isolated from TRIzol (Invitrogen) using the Direct-zol RNA Miniprep Plus Kit (Zymo Research) with DNase I treatment according to the manufacturer's directions. These RNA samples were then subject to barcode sequencing as described above.

Polysome profiling

To examine the effect of CNOT1, PSMA4, RPS19, TCP1 and FLUC depletion on global translation, polysome profiling was performed with the five cell lines from 'CRISPR–Cas9 mediated gene knockout for polysome profiling' (Supplementary Methods). Polysome profiling was performed similar to the polysome ReLiC screen, except that each sample was collected from one 10-cm dish at ~60% confluence. To examine whether GCN1 affects the level of RNase-resistant disomes during HHT treatment, polysome profiling was performed with four different samples: 293T cells expressing sgGCN1 and sgFLUC from 'CRISPR–Cas9 mediated gene knockout for RNA-seq' (Supplementary Methods) after 1 week of Cas9 induction, treated for 1 h with 1 µM HHT or DMSO. Polysome profiling was performed similar to the individual gene perturbations from above, except, before loading onto sucrose gradients, lysates were incubated with or without 1 U micrococcal nuclease per µg RNA and 5 µM CaCl₂ at room temperature for 1 h. Micrococcal nuclease digests were quenched by adding 5 µM EGTA before loading on sucrose gradients.

RNA sequencing

Total RNA was isolated using the Direct-zol RNA Miniprep kit (Zymo). PolyA⁺ mRNA was extracted from total RNA using Oligo d(T)25 Magnetic Beads (NEB). A total RNA input of 2 µg and 25 µl Oligo d(T)25 beads were used per sample. Sequencing libraries were generated from polyA⁺ mRNA using the NEBNext Ultra II Directional RNA Library Prep Kit (NEB) and sequenced on a NextSeq 2000 (Illumina) with 2 × 50 cycle paired-end reads.

Ribosome profiling

Ribosome profiling was performed with four different samples: 293T cells expressing sgGCN1 and sgFLUC from 'CRISPR–Cas9 mediated gene knockout for RNA-seq' (Supplementary Methods) after 1 week of Cas9 induction, treated for 1 h with 1 µM HHT or DMSO. For each sample, we used one 15-cm plate of cells, seeded to ~40% confluence at collection. The ribosome profiling protocol was adapted from ref. 57 with the following modifications. For sample collection, we removed medium from each plate and flash froze samples by placing the plate in liquid nitrogen and transferring it to -80 °C until lysis. We performed nuclelease footprinting treatment by adding 80 U RNase I (Invitrogen AM2294) to 25 µg of RNA. We gel purified ribosome-protected fragments with length between 26 and 34 nucleotides using RNA

oligonucleotide size markers. We used polyA tailing instead of linker ligation following previous studies^{58,59}. Libraries were sequenced on an Illumina NextSeq 2000 in 50-bp single-end mode.

Immunoblotting

sgGCN1- and sgFLUC-expressing cell lines hsPN309 and hsPN313 were passaged for 1 week with 2 µg ml⁻¹ doxycycline to deplete GCN1. These lines were subsequently incubated with HHT, anisomycin or DMSO at the indicated concentrations for 60 min before collection. If indicated, cells were pretreated with nilotinib for 30 min before starting HHT treatment. HHT, anisomycin and nilotinib were dissolved in DMSO. Cells were rinsed with PBS and lysed in RIPA buffer. Lysates were kept on ice during preparation and clarified by centrifugation at 21,000g (15,000 rpm) for 10 min. After clarification, supernatants were boiled in Laemmli loading buffer containing DTT, and western blots were performed using standard molecular biology procedures (unprocessed blot images in source data for Fig. 5 and Extended Data Fig. 5). Proteins were resolved with 4–20% Criterion TGX protein gels (Bio-Rad) and transferred to PVDF membranes using a Trans-Blot Turbo Transfer System (Bio-Rad). Membranes were blocked with 5% BSA (Thermo) in TBST and incubated with primary antibodies overnight at 4 °C with gentle rocking. Blots were washed with TBST and then incubated with secondary antibodies diluted in TBST with 5% BSA for 1 h at room temperature with gentle rocking. Membranes were washed again with TBST, developed using SuperSignal West Femto Maximum Sensitivity Substrate (Thermo) and imaged on a ChemiDoc MP Imaging System (Bio-Rad).

Flow cytometry

After dissociating cells from culture dishes, they were pelleted and resuspended in Dulbecco's PBS (Gibco, 14190-144) supplemented with 5% FBS. Forward scatter, side scatter, BFP fluorescence (BV421), YFP fluorescence (FITC) and mCherry fluorescence (PE-Texas Red) were measured for 10,000 cells in each sample using a BD FACSymphony or Fortessa instrument.

Computational analyses

Preprocessing steps for high-throughput sequencing analyses were implemented as Snakemake⁶⁰ workflows run within Singularity containers on an HPC cluster. Python (version 3.9.15) and R (version 4.2.2) programming languages were used for all analyses unless mentioned otherwise. Analysis of RNA-seq, ribosome profiling and Perturb-seq data as well as gene ontology analyses are described in Supplementary Methods.

Barcode-to-insert assignment

Raw data from insert–barcode linkage sequencing are in FASTQ format. Barcode and sgRNA insert sequences were extracted from corresponding reads and counted using awk; sgRNA inserts and corresponding barcodes were omitted if the sequenced sgRNA insert was not present in the designed sgRNA library (oAS1899). The remaining barcodes were aligned against themselves by first building an index with bowtie2-build with default options and then aligning using Bowtie 2 with options ‘-L 19 -N 1 --allow-noc -no-unal -f’. Self-alignment was used to exclude barcodes that were linked to distinct inserts or ones that were linked to the same insert but were aligned against each other with Bowtie 2 (presumably due to sequencing errors). In the latter case, the barcode with the lower count was discarded in filter_barcodes.ipynb. The final list of insert–barcode pairs with a minimum of five reads was written as a comma-delimited .csv file for aligning barcodes from genomic DNA and mRNA sequencing below.

Barcode counting in genomic DNA and mRNA

Raw data from sequencing barcodes in genomic DNA and mRNA are in FASTQ format. Barcode and UMI sequences were extracted from

corresponding reads, counted using awk and assigned to reporters based on their unique 6 × N identifier. Only distinct barcode–UMI combinations for which the barcode was present in the filtered barcodes .csv file from linkage sequencing were retained. The number of UMIs per barcode and associated insert were written to a .csv file for subsequent analyses in R. Only barcodes with a minimum of 20 UMIs were used for analysis. Barcode counts from pairs of samples were used to run MAGeCK²⁵ with ‘--additional-rra-parameters’ set to ‘--min-number-goodsgRNA 3’. sgRNAs without a minimum of 20 UMI in one of the compared samples were set to 20 UMI counts before running MAGeCK.

Chemicals

ISRB (SML0843) was obtained from Sigma. HHT (FH15974) was sourced from Biosynth. Anisomycin (A50100), hygromycin B (H75020) and puromycin dihydrochloride (P33020) were purchased from Research Products International. Nilotinib (A8232) was acquired from ApexBio. Vemurafenib (S1267) was obtained from SelleckChem. SMG1i (HY-124719), GCN2iB (HY-112654) and eFT226 (HY-112163) were all purchased from MedChemExpress. Finally, 4E1RCat (S7370) was obtained from SelleckChem.

Antibodies

The anti-p38 MAPK antibody (8690, RRID AB_10999090) was obtained from Cell Signaling Technology and used at a 1:1,000 dilution. The anti-phospho-p38 (Thr180 and Tyr182) antibody (690201, RRID AB_2801132) was sourced from BioLegend and used at a 1:1,000 dilution. The anti-GCN1 antibody (A301843AT, RRID AB_1264319) was purchased from Bethyl and used at a 1:1,000 dilution. Secondary antibodies included goat anti-rabbit IgG (H + L)–HRP conjugate (1721019, RRID AB_11125143) and goat anti-mouse IgG (H + L)–HRP conjugate (1721011, RRID AB_11125936), both sourced from Bio-Rad and used at a 1:5,000 dilution.

Statistics and reproducibility

All protein immunoblotting and DNA electrophoresis experiments were repeated at least three times, and representative gel images are shown.

Reporting summary

Further information on research design is available in the Nature Portfolio Reporting Summary linked to this article.

Data availability

All high-throughput sequencing data are publicly available in the NCBI SRA database under BioProject PRJNA1059490. SRA accession numbers with sample annotations are provided in Supplementary Table 5. All other data are publicly available at https://github.com/rasilab/nugent_2024. Source data are provided with this paper.

Code availability

All software used in this study is publicly available as Docker images at <https://github.com/orgs/rasilab/packages>. Data analysis and visualization code are publicly available at https://github.com/rasilab/nugent_2024. Information not included in the study can be publicly requested at https://github.com/rasilab/nugent_2024/issues.

References

56. Natsume, T., Kiyomitsu, T., Saga, Y. & Kanemaki, M. T. Rapid protein depletion in human cells by auxin-inducible degron tagging with short homology donors. *Cell Rep.* **15**, 210–218 (2016).
57. Ingolia, N. T., Brar, G. A., Rouskin, S., McGeachy, A. M. & Weissman, J. S. The ribosome profiling strategy for monitoring translation in vivo by deep sequencing of ribosome-protected mRNA fragments. *Nat. Protoc.* **7**, 1534–1550 (2012).

58. Ingolia, N. T., Ghaemmaghami, S., Newman, J. R. S. & Weissman, J. S. Genome-wide analysis in vivo of translation with nucleotide resolution using ribosome profiling. *Science* **324**, 218–223 (2009).
59. Lee, S. et al. Global mapping of translation initiation sites in mammalian cells at single-nucleotide resolution. *Proc. Natl Acad. Sci. USA* **109**, E2424–E2432 (2012).
60. Köster, J. & Rahmann, S. Snakemake—a scalable bioinformatics workflow engine. *Bioinformatics* **28**, 2520–2522 (2012).

Acknowledgements

We thank members of the Subramaniam laboratory, the Basic Sciences Division and the Computational Biology Program at Fred Hutch for assistance with the project and discussions. We thank A. Geballe, C. Lapointe, A. Rajan and B. Zid for feedback on the paper. This research was funded by NIH R35 GM119835 (A.R.S.), NSF MCB 1846521 (A.R.S.), NIH T32 GM008268 (P.J.N.), NIH R37 CA230617 (A.C.H.), NIH R01 CA276308 (A.C.H.) and NIH GM135362 (A.C.H.). This research was supported by the Genomics and Flow Cytometry Shared Resources of the Fred Hutch/University of Washington Cancer Consortium (P30 CA015704) and Fred Hutch Scientific Computing (NIH grants S10-OD-020069 and S10-OD-028685). The funders had no role in study design, data collection and analysis, decision to publish or preparation of the manuscript.

Author contributions

P.J.N. designed research, performed experiments, analyzed data and wrote the paper. H.P. performed experiments. C.L.W., J.N.Y. and A.C.H.

assisted with polysome fractionation experiments. S.S. and S.C.L. performed experiments on the U937 cell line. C.B., G.Q. and K.Y.C. performed gene ontology analyses. A.R.S. conceived the project, designed research, analyzed data, wrote the paper, supervised the project and acquired funding.

Competing interests

The authors declare no competing interests.

Additional information

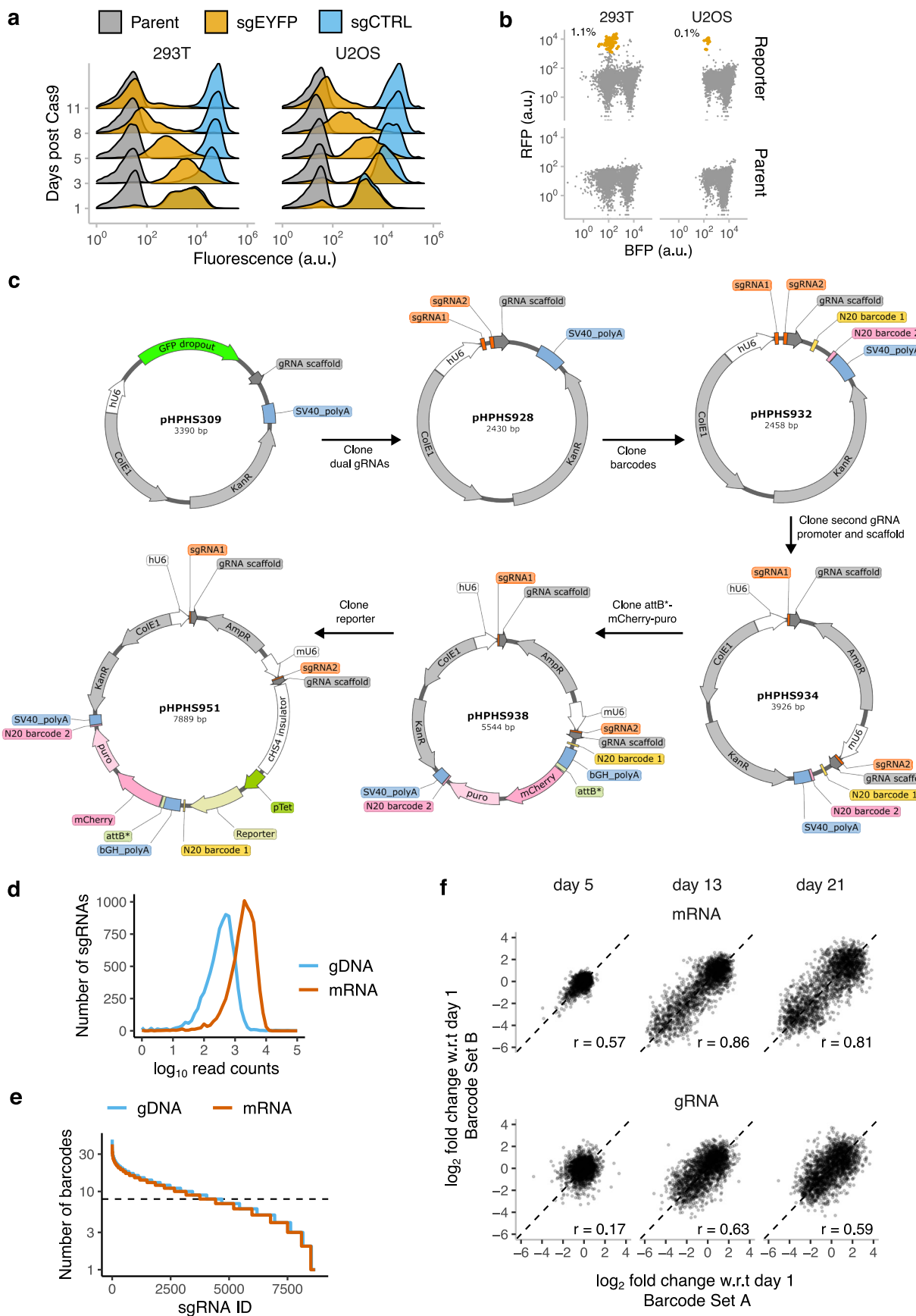
Extended data is available for this paper at <https://doi.org/10.1038/s41592-025-02702-6>.

Supplementary information The online version contains supplementary material available at <https://doi.org/10.1038/s41592-025-02702-6>.

Correspondence and requests for materials should be addressed to Arvind Rasi Subramaniam.

Peer review information *Nature Methods* thanks Junyue Cao and the other, anonymous, reviewer(s) for their contribution to the peer review of this work. Primary Handling Editor: Lei Tang, in collaboration with the *Nature Methods* team.

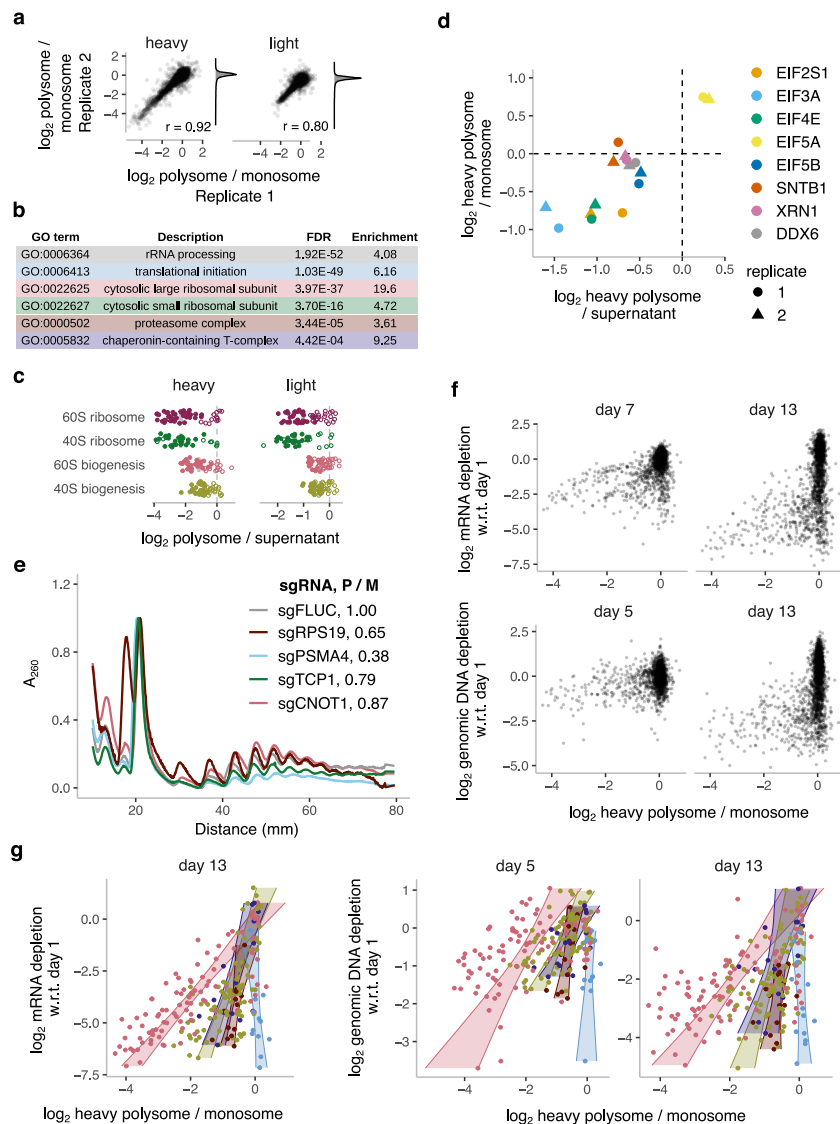
Reprints and permissions information is available at www.nature.com/reprints.



Extended Data Fig. 1 | See next page for caption.

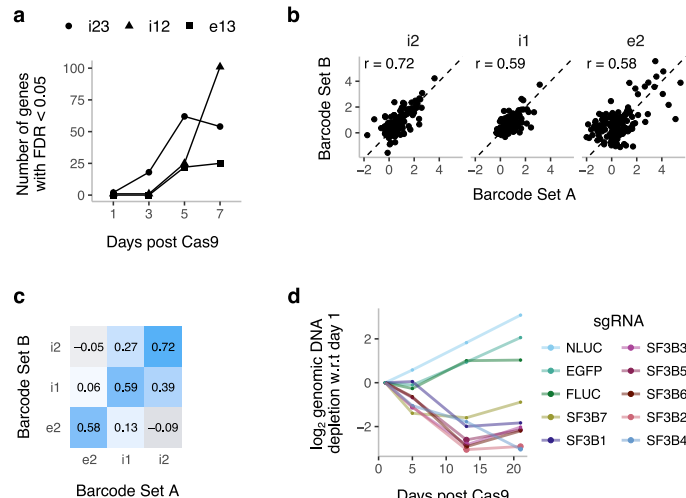
Extended Data Fig. 1 | ReLiC library design and validation. **a.** Validation of Cas9 activity in U2OS. sgEYFP and sgCTRL are single guide RNAs targeting EYFP or a non-targeting control, respectively. Each histogram represents fluorescence of 10,000 cells as measured by flow cytometry. 'Days post Cas9' refers to days after addition of doxycycline to induce Cas9 expression. **b.** Comparison of integration into 293T and U2OS landing pads. BFP and mCherry fluorescence were measured for 10,000 cells, depicted as individual points. Proportion of cells that are mCherry+ and BFP- (orange points) is indicated. No cells in either

parental control are mCherry+ and BFP-. **c.** Depiction of cloning scheme for ReLiC library and reporters. **d.** Distribution of sgRNA-linked barcode counts in mRNA and genomic DNA. **e.** Number of unique barcodes linked to each sgRNA in ReLiC library. **f.** Correlation between distinct barcode sets in ReLiC fitness screens. Each point represents a unique sgRNA pair from the ReLiC RBP library. For each sgRNA pair, individual linked barcodes were randomly partitioned into two sets of equal size (or to within a barcode for odd number of detected barcodes). r refers to Pearson correlation coefficient between the barcode sets.



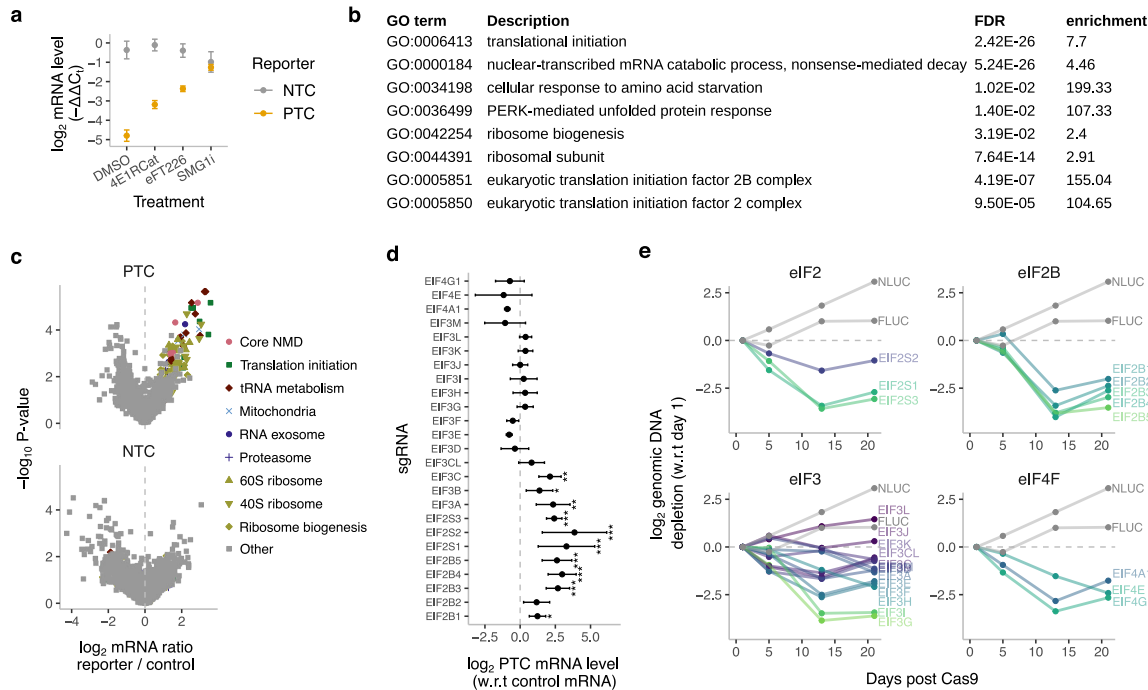
Extended Data Fig. 2 | Polysome ReLiC screen for regulators of mRNA translation. **a.** Correlation between replicates. Points represent individual sgRNAs in the ReLiC library. Polysome to monosome ratios are median-centered across sgRNAs in the library. r refers to Pearson correlation coefficient. **b.** Gene ontology analysis of perturbations that decrease heavy polysome to monosome ratio. Gene ontology analysis performed using GOrilla [Eden2009] and a subset of enriched terms representative of specific gene classes are shown. **c.** Change in polysome to supernatant ratio for ribosomal protein and ribosome biogenesis genes. Closed circles correspond to gene hits ($FDR < 0.05$ with 3 or more concordant sgRNAs). **d.** Comparison of heavy polysome to monosome and

heavy polysome to supernatant ratios for selected translation-related factors. **e.** Polysome profiles of cell lines depleted of screen hits Profiles are normalized by 80S peak height. P/M indicates ratio of area under the curve for polysome fractions to monosome fractions. **f.** Comparison of heavy polysome to monosome ratio with growth fitness measured by mRNA and genomic DNA barcode sequencing. **g.** Comparison of heavy polysome to monosome ratio with growth fitness measured by genomic DNA barcode sequencing for gene knockouts in specific groups. Points correspond to genes targeted in the ReLiC-RBP library. Shaded areas correspond to 95% confidence intervals for a linear fit of polysome to monosome ratio to growth fitness within each gene group.



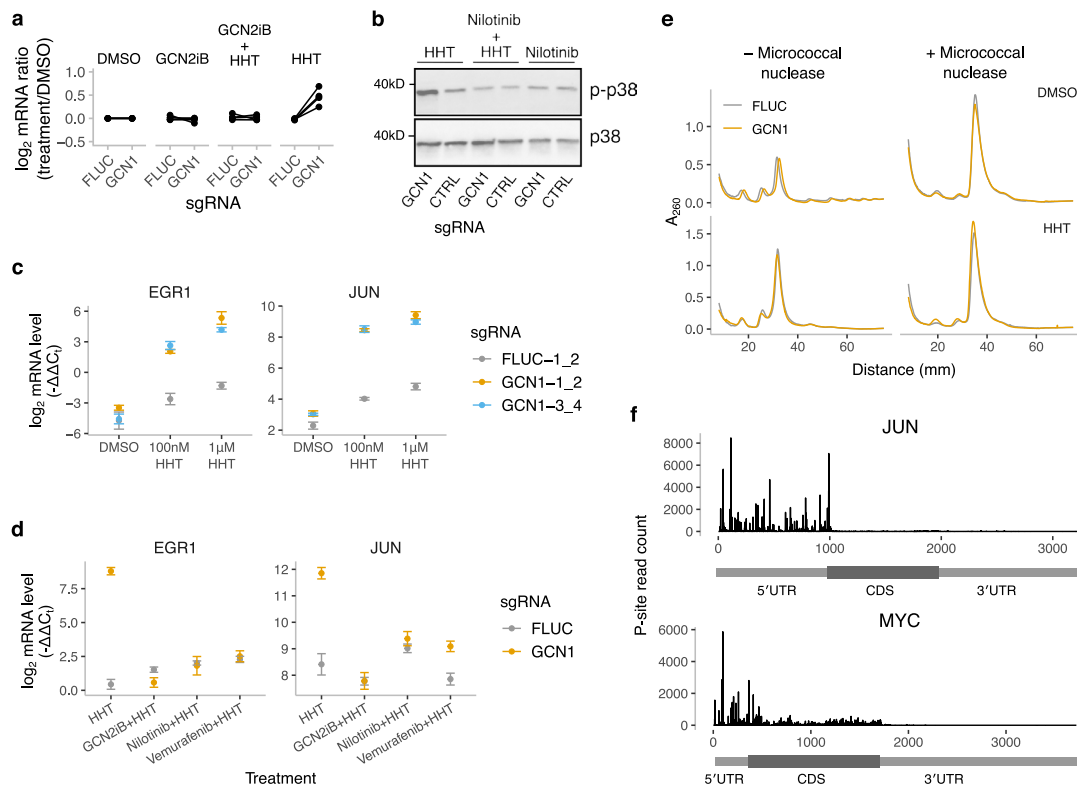
Extended Data Fig. 3 | Isoform-specific splicing screen using ReLiC. **a.** Number of gene hits that increase the level of the indicated reporter isoform on various days after Cas9 induction. **b.** Correlation between barcode sets. For each sgRNA, individual linked barcodes were randomly partitioned into two sets, as in Extended Data Fig. 1f. Each point represents a unique gene that was classified as

a hit either with barcode Set A or barcode set B. **r** refers to Pearson correlation coefficient between barcode sets. **c.** Correlation between relative levels of different mRNA isoforms. Values represent Pearson correlation coefficients for pairwise comparison between the two barcode sets in **b**. **d.** Depletion of genomic DNA barcodes corresponding to SF3b complex subunits after Cas9 induction.



Extended Data Fig. 4 | Dissecting mRNA quality control using ReLiC.
a. Validation of β -globin NMD reporters. Vertical axis represents $-\Delta\Delta C_t$ value of indicated reporter mRNA relative to mCherry-Puro control mRNA. Error bars denote standard error of qPCR across 3 technical replicates. **b.** Gene ontology analysis of perturbations that increase PTC reporter mRNA levels. **c.** Volcano plot of reporter mRNA levels with dual barcode screen. Each point corresponds to a gene targeted by the ReLiC library. Marker shape and color denotes one of highlighted gene groups. Genes with FDR < 0.05 and belonging to one of the

highlighted groups are listed in the legend. Vertical axis indicates P-values from a permutation test as calculated by MAGeCK. **d.** PTC reporter mRNA levels for individual translation initiation complex subunits. Error bars denote standard deviation across all detected sgRNAs for that gene. Vertical axis indicates P-values from a permutation test as calculated by MAGeCK; ***: $P < 0.001$, **: $0.001 < P < 0.01$, *: $0.01 < P < 0.05$; all other genes have $P > 0.05$. **e.** Growth fitness after depletion of translation initiation complex subunits.



Extended Data Fig. 5 | GCN1 regulates cellular responses to an anti-leukemic drug. **a.** Regulation of EYFP reporter levels by GCN2 after HHT treatment. Cell lines were treated with 1 μM GCN2i for 30m prior to 6h of 1 μM HHT treatment. Vertical axis represents the ratio of EYFP reporter barcode counts during indicated treatment compared to the DMSO-treated control in cells expressing indicated sgRNA. **b.** ZAK-dependent phosphorylation of p38 in HEK293T cells +/- GCN1 treated with HHT. Cells were treated with nilotinib (1 μM) or DMSO for 30 minutes prior to addition of homoharringtonine (1 μM) treatment or DMSO for 1 hour. **c.** GCN1-dependent changes to endogenous mRNA expression after HHT treatment in U937 cells +/- GCN1. U937 cell lines were treated with indicated HHT concentrations or DMSO as a vehicle control for 6h. Vertical axis represents $-\Delta\Delta Ct$ value of either EGR1 or JUN mRNA relative to GAPDH mRNA as measured by RT-qPCR. Error bars denote standard error of qPCR across 3 technical replicates.

d. Regulation of endogenous mRNA expression by GCN2 and ZAK after HHT treatment. Cell lines were treated with 1 μM GCN2i or 1 μM of the ZAK inhibitors nilotinib and vemurafenib for 30m prior to 6h of 1 μM HHT treatment. Vertical axis represents $-\Delta\Delta Ct$ value of either EGR1 or JUN mRNA relative to GAPDH mRNA as measured by RT-qPCR. Error bars denote standard error of qPCR across 3 technical replicates. **e.** Polysome profiles of GCN1-depleted and control cell lines after HHT treatment. Cells were treated with 1 μM HHT or DMSO for 1 hour prior to lysis. Polysome lysates were digested with 1 U micrococcal nuclease / μg of RNA prior to sucrose gradient sedimentation. **f.** Ribosome P-site density on JUN and MYC mRNAs from previous ribosome profiling studies using harringtonine or lactimidomycin to arrest initiating ribosomes.

Reporting Summary

Nature Portfolio wishes to improve the reproducibility of the work that we publish. This form provides structure for consistency and transparency in reporting. For further information on Nature Portfolio policies, see our [Editorial Policies](#) and the [Editorial Policy Checklist](#).

Statistics

For all statistical analyses, confirm that the following items are present in the figure legend, table legend, main text, or Methods section.

n/a Confirmed

- The exact sample size (n) for each experimental group/condition, given as a discrete number and unit of measurement
- A statement on whether measurements were taken from distinct samples or whether the same sample was measured repeatedly
- The statistical test(s) used AND whether they are one- or two-sided
Only common tests should be described solely by name; describe more complex techniques in the Methods section.
- A description of all covariates tested
- A description of any assumptions or corrections, such as tests of normality and adjustment for multiple comparisons
- A full description of the statistical parameters including central tendency (e.g. means) or other basic estimates (e.g. regression coefficient) AND variation (e.g. standard deviation) or associated estimates of uncertainty (e.g. confidence intervals)
- For null hypothesis testing, the test statistic (e.g. F , t , r) with confidence intervals, effect sizes, degrees of freedom and P value noted
Give P values as exact values whenever suitable.
- For Bayesian analysis, information on the choice of priors and Markov chain Monte Carlo settings
- For hierarchical and complex designs, identification of the appropriate level for tests and full reporting of outcomes
- Estimates of effect sizes (e.g. Cohen's d , Pearson's r), indicating how they were calculated

Our web collection on [statistics for biologists](#) contains articles on many of the points above.

Software and code

Policy information about [availability of computer code](#)

| | |
|-----------------|---|
| Data collection | High-throughput sequencing data were collected using the Illumina NextSeq 2000 platform. Flow cytometry data were collected using BD FACSDiva software. |
| Data analysis | Data were analyzed using Bowtie2 (v2.4.5), MAGECK (v0.5.9), STAR (v2.7.11a), Python (v3.9.15), and R (v4.2.2). All code is available at https://github.com/rasilab/nugent_2024 . |

For manuscripts utilizing custom algorithms or software that are central to the research but not yet described in published literature, software must be made available to editors and reviewers. We strongly encourage code deposition in a community repository (e.g. GitHub). See the Nature Portfolio [guidelines for submitting code & software](#) for further information.

Data

Policy information about [availability of data](#)

All manuscripts must include a [data availability statement](#). This statement should provide the following information, where applicable:

- Accession codes, unique identifiers, or web links for publicly available datasets
- A description of any restrictions on data availability
- For clinical datasets or third party data, please ensure that the statement adheres to our [policy](#)

All high-throughput sequencing data is publicly available in the NCBI SRA database under BioProject PRJNA1059490. All other data are available in a public GitHub repository (https://github.com/rasilab/nugent_2024).

Human research participants

Policy information about [studies involving human research participants](#) and [Sex and Gender in Research](#).

Reporting on sex and gender

N/A

Population characteristics

N/A

Recruitment

N/A

Ethics oversight

N/A

Note that full information on the approval of the study protocol must also be provided in the manuscript.

Field-specific reporting

Please select the one below that is the best fit for your research. If you are not sure, read the appropriate sections before making your selection.

Life sciences Behavioural & social sciences Ecological, evolutionary & environmental sciences

For a reference copy of the document with all sections, see nature.com/documents/nr-reporting-summary-flat.pdf

Life sciences study design

All studies must disclose on these points even when the disclosure is negative.

Sample size

Library sizes were chosen such that each sgRNA insert was covered by an average of 8 barcodes and these libraries were maintained at >100X coverage throughout the cloning and selection steps. In each case, sample size was appropriate based on the consistency of measurable differences between groups.

Data exclusions

No data were excluded from analyses.

Replication

The ReLiC polysome screen was performed in technical duplicate. qPCR experiments were performed as 3 technical replicates. All attempts at replication were successful and are reported in the manuscript.

Randomization

Samples were not assigned to different cohorts or study arms, so randomization would not apply to the work done here. All samples were treated the same.

Blinding

No group allocation or blinding was performed in this study.

Reporting for specific materials, systems and methods

We require information from authors about some types of materials, experimental systems and methods used in many studies. Here, indicate whether each material, system or method listed is relevant to your study. If you are not sure if a list item applies to your research, read the appropriate section before selecting a response.

Materials & experimental systems

- | | |
|-------------------------------------|---|
| n/a | Involved in the study |
| <input type="checkbox"/> | <input checked="" type="checkbox"/> Antibodies |
| <input type="checkbox"/> | <input checked="" type="checkbox"/> Eukaryotic cell lines |
| <input checked="" type="checkbox"/> | <input type="checkbox"/> Palaeontology and archaeology |
| <input checked="" type="checkbox"/> | <input type="checkbox"/> Animals and other organisms |
| <input checked="" type="checkbox"/> | <input type="checkbox"/> Clinical data |
| <input checked="" type="checkbox"/> | <input type="checkbox"/> Dual use research of concern |

Methods

- | | |
|-------------------------------------|--|
| n/a | Involved in the study |
| <input checked="" type="checkbox"/> | <input type="checkbox"/> ChIP-seq |
| <input type="checkbox"/> | <input checked="" type="checkbox"/> Flow cytometry |
| <input checked="" type="checkbox"/> | <input type="checkbox"/> MRI-based neuroimaging |

Antibodies

Antibodies used

p38 MAPK (CST 8690; RRID:AB_10999090), Phospho-p38 MAPK (Thr180/Tyr182) (Biolegend 690201; RRID:AB_2801132), GCN1 (Bethyl A301843AT; RRID:AB_1264319), β-actin (Sigma A5441; RRID:AB_476744)

Validation

Manufacturer for each antibody states that they are validated for the reported human targets in Western blots.

Eukaryotic cell lines

Policy information about [cell lines and Sex and Gender in Research](#)

Cell line source(s)

The HEK293T cell line was obtained from ATCC (ATCC CRL-3216; RRID:CVCL_0063). The U2OS cell line was also obtained from ATCC (ATCC HTB-96; RRID:CVCL_0042). The U937 (RRID:CVCL_0007) cell line was obtained from the Jerald Radich Lab (Fred Hutchinson Cancer Center).

Authentication

HEK293T and U937 cell line identities were confirmed by short tandem repeat analysis. U2OS cell line identity was not authenticated.

Mycoplasma contamination

All cell lines were confirmed negative for mycoplasma contamination.

Commonly misidentified lines
(See [ICLAC](#) register)

No commonly misidentified lines were used in this study.

Flow Cytometry

Plots

Confirm that:

- The axis labels state the marker and fluorochrome used (e.g. CD4-FITC).
- The axis scales are clearly visible. Include numbers along axes only for bottom left plot of group (a 'group' is an analysis of identical markers).
- All plots are contour plots with outliers or pseudocolor plots.
- A numerical value for number of cells or percentage (with statistics) is provided.

Methodology

Sample preparation

HEK293T cell lines were dissociated from culture dish using trypsin, then resuspended in PBS.

Instrument

BD Fortessa X50

Software

Data was collected using BD FacsDiva software. Data were analyzed using custom R scripts that are available in a public GitHub repository (https://github.com/rasilab/nugent_2024).

Cell population abundance

N/A

Gating strategy

No gating was performed.

Tick this box to confirm that a figure exemplifying the gating strategy is provided in the Supplementary Information.